



MSc thesis

Application of non-invasive MR imaging for the mouse brain water mobility and con- tent assessment

Paula Melero Martinez, BS

Direct advisor at CTN KU: Ryszard S. Gomolka, PhD

Supervisor at CTN KU: Yuki Mori, PhD

Supervisor at NBI KU: Liselotte Jauffred, PhD

Submitted: May 19, 2022

Contents

1	Introduction	5
1.1	The waste clearance mechanisms with fluid compartments in the brain	5
1.2	Glymphatic system and general factors affecting the glymphatic function	5
1.3	Glymphatic system and AQP4 water channel	6
1.4	Neuroimaging and role of non-invasive methods in understanding glymphatics	8
1.5	Impact of noninvasive acquisition on the glymphatic studies	9
1.6	Aims and summary of current work	10
2	Theoretical background for MR imaging	11
2.1	Proton relaxation times	11
2.1.1	T1 relaxation time	11
2.1.2	T2 relaxation time	12
2.1.3	T2* relaxation time	13
2.1.4	Gadolinium T1 and T2 shortening	13
2.2	MR sequences and signals	14
2.2.1	Spin-echo	14
2.2.2	Gradient-recalled echo	14
2.2.3	Multi-slice technique	16
2.2.4	Comparison SE vs. GRE	17
2.2.5	Echo-planar Imaging	18
2.2.6	DWI	20
2.3	Dixon method	21
2.3.1	Basis	21
2.3.2	Signal modelling	22
2.3.3	Two-point Dixon	23
2.3.4	Three-point Dixon	24
2.3.5	Phase unwrapping	24
3	Methods	26
3.1	In-vivo imaging	26
3.2	In-vivo images analysis	27
3.2.1	Theoretical perspective of DWI images calculation	28
3.2.2	Dixon calculation	29
3.2.3	DWI and Dixon ROI setting	29
3.3	Ex-vivo imaging	30
3.3.1	Water phantom with gadolinium contrast	31
3.3.2	Dixon phantom with gadolinium contrast.	31
3.3.3	Dixon phantom without gadolinium contrast	33

3.4	Processing of the phantom images	36
3.4.1	T1 mapping using RARE variable TR	37
3.4.2	Radiofrequency transmit field inhomogeneity correction (B_1^+ -correction)	38
3.4.3	T2 mapping	39
3.4.4	Dixon images calculation	40
3.5	Statistical analysis	41
3.5.1	Statistical analysis: in-vivo	41
3.5.2	Correlation between Dixon and DWI in-vivo	41
3.5.3	Statistical analysis: ex-vivo	42
4	Results	43
4.1	In-vivo imaging	43
4.1.1	DWI	43
4.1.2	Dixon	45
4.2	Region-wise DWI-Dixon correlation	47
4.3	Ex-vivo imaging	47
4.3.1	Water phantom with gadolinium contrast	47
4.3.2	Dixon phantom with gadolinium contrast	53
4.3.3	Dixon phantom without gadolinium contrast	63
5	Discussion	72
6	Conclusions	76

Abstract

Glymphatic system comprises a brain-wide metabolite and waste transport pathway involving cerebral-spinal fluid (CSF)/interstitial fluid (ISF) exchange, and is facilitated by astrocytic aquaporin-4 (AQP4) channel. However, magnetic resonance imaging (MRI) is the most applicable for the whole brain *in-vivo* glymphatics assessment, to date applied methods based on invasive tracers application altering CSF dynamics. Therefore current work aimed to analyze and validate a fully non-invasive *in-vivo* glymphatic 9.4 Tesla MRI protocol in 9 AQP4 knock-out and 9 wild-type littermate animals of 10 – 15 weeks age. The protocol was designed at the Center for Translational Neuromedicine and based on standard and widely available diffusion-weighted imaging (DWI) and multiecho gradient-recalled echo (GRE) Dixon for the brain free water mobility and fat/water content assessment, respectively. In addition, *ex-vivo* validation of the design Dixon approach was performed in dedicated phantoms of authors' own design.

Summarizing, current work confirms suitability of both DWI and intravoxel incoherent motion (IVIM)-DWI as well as Dixon imaging for assessment of the brain free water mobility as well as the fat/water brain content. By highlighting existence of slow water diffusion differences among parenchymal brain regions, as well as differences in the brain water content, this analysis showed ability of analyzed non-invasive MRI approach in differentiating normal conditions from those resulting from genetically silencing of the main brain water channel AQP4. Moreover, supplementary phantom imaging brought up a possibility for further fine-tuning of a dedicated MRI approach to glymphatics, and opened a path for further translational MRI protocols.

Keywords: aquaporin-4 (AQP4) channel, diffusion-weighted imaging (DWI), gradient-recalled echo (GRE)-based Dixon

1 Introduction

1.1 The waste clearance mechanisms with fluid compartments in the brain

The human brain represents $\approx 2\%$ of the adult human body mass. Still, the brain possesses a high energy demand such as 20 to 25% of total body glucose and around 20% of oxygen [1]. In the process of high energy consumption, considerable amounts of wastes and biological debris are generated. To maintain the brain's health, it requires having a way of clearing out the debris. The brain has a high structural complexity, formed of neuronal cells, oligodendrocytes and astrocytes, and is surrounded by a cerebral-spinal fluid (CSF). Despite the brain's complexity and high metabolic rate [1, 2] no specialized structure or tissue has yet been found to have the same function in the brain as the lymphatic system in the body. Such structure should enable clearance of metabolites (such as amyloid- β) and drain the excess of interstitial fluid (ISF) [3]. For a long time, the role of CSF was attributed mainly as mechanical and neuroprotective, but with the advent of novel *in-vivo* imaging and molecular approaches, the role of CSF was explicated to go beyond the traditionally considered [4, 5]. The CSF production, reabsorption, and circulation mechanisms were also found more complex than previously believed [6]. By mixing with the brain's ISF [7], CSF plays a key role in electrolyte balance, distribution of energy metabolites, bioactive molecules, and elimination of catabolites [8, 9]. As the brain parenchyma is separated from the blood pool, the question appeared on how the exchange of those compounds takes place? This question was of high importance, especially that the brain's fluid compartments follow its complexity, and consist of interstitial fluid (12 – 20%) and intracellular fluid (60 – 68%) included in the brain parenchyma, the blood from penetrating arteries and veins (10%) and finally CSF (10%) filling the lateral, third and fourth ventricles and surrounding the brain parenchyma [10, 11].

1.2 Glymphatic system and general factors affecting the glymphatic function

About 10 year ago, a brain-wide anatomical and functional pathway was identified to facilitate the clearance of interstitial solutes from the brain [8]. This clearance pathway has been named the glymphatic system because of its dependence on the glia cells and its analogous function to the lymphatic system. The glymphatic system involves CSF/ISF exchange [7] assisted by three key elements: 1) a para-arterial CSF influx route, 2) a para-venous ISF efflux route, and 3) aquaporin-4 (AQP4) water channel located mainly at the astrocytic end-feet. The primary role of AQP4 has been suggested

to facilitate the entrance of CSF to the brain parenchyma and the efflux of ISF from the brain parenchyma (Figure 1). Multiple factors have been observed affecting the normal function and grade of activity of the glymphatic system and subsequent drainage of metabolic waste products. The state of consciousness [12] has been pointed out as one of the major driving force of the glymphatic system. A larger CSF flow along perivascular space (PVS) entering the brain was observed in asleep and anesthetized mice compared to awake subjects and increased clearance of amyloid- β was seen during sleep state [7]. Head-body positioning [13], alcohol consumption [14] and voluntary activity [15] are among other factors that has been described affecting the brain waste removal ability of the glymphatic system.

1.3 Glymphatic system and AQP4 water channel

As described above, AQP4 channels also have been considered as an important factor as CSF/ISF driving force. To date, research on the glymphatic transport and role of AQP4 channel was predominantly performed in anesthetized and awake rodents [16, 17, 18, 19]. The key element of the glymphatic system was described as the transmembrane AQP4 channel, discovered by Agre et al. [20]. The glymphatic system begun to be a subject of increasing interest in the scientific community since 2012 (see Figure 2). The first discovery report of glymphatic system from Illif et al. [8] described markedly reduced CSF tracers movement into the brain parenchyma of mice lacking AQP4 water channel, compared to their wild-type (WT) littermates. In this work, they showed that a large proportion ($> 40\%$) of subarachnoid CSF infiltrated into the brain parenchyma from the PVS surrounding the penetrating arteries (see Figure 1). Once the CSF is in the interstitial space, exchange of CSF and ISF occurs carrying away the waste products such as amyloid- β . These ISF and waste products are cleared out from the brain along para-venous routes. From here, metabolites and ISF may enter the bloodstream to further be cleared out at the liver or kidneys. However, AQP4 knock-out (KO) animals showed a CSF influx reduction in the brain parenchyma and $\approx 70\%$ reduction in the metabolites clearance [8]. This finding is one of the evidence that influx and efflux of CSF and ISF across the brain parenchyma is facilitated by the AQP4 water channels.

AQP4 water channels are mainly located at the end-feet of astrocytes, adjacent to capillaries, neurons and neuronal synapses [8]. AQP4 are anchored to the cell membrane of astrocytes through a dystrophin protein complex [22]. Astrocytes are important for maintaining water balance along with ion homeostasis. In the mammalian brain there are more than 5 times more astrocytes than neurons [22]. The highest density of AQP4 is close to the capillary [22], and polarized towards the vasculature, but also in the brain regions associated with CSF flow, including ventricular and cisternal spaces

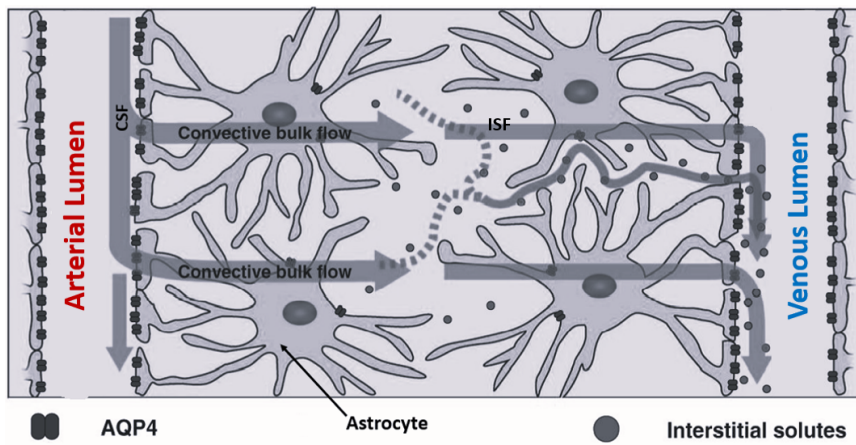


Figure 1: Schematic representation of the glymphatic system. CSF enters the brain parenchyma facilitated by AQP4 channels. Exchange between CSF and ISF occurs in the interstitial space. Efflux of ISF with the waste products to the para-venous space is mediated by AQP4 channels [21]. Modified Figure 5B from [8]

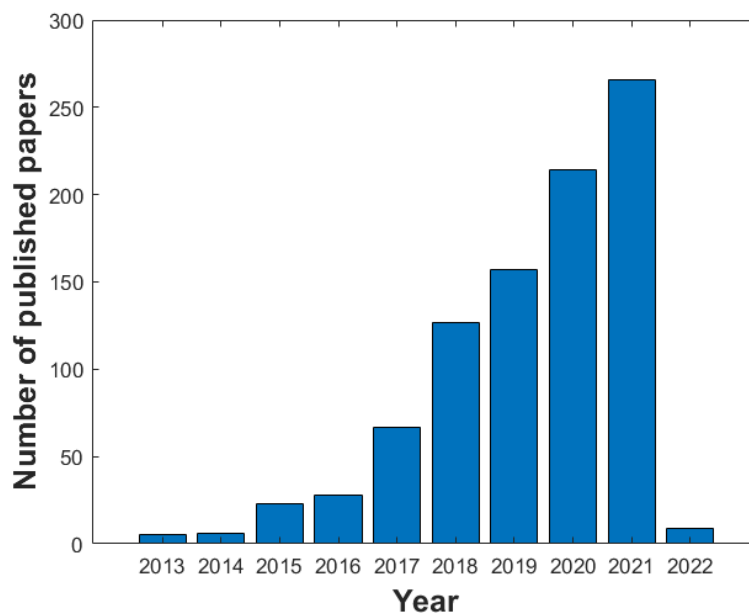


Figure 2: Publications listed in Pubmed since 2012 under the search term 'glymphatic system'. [pubmed.ncbi.nlm.nih.gov, accessed: May 2022]

[23]. However, the lower density of AQP4 channels close to neurons is compensated by large astrocyte end-feet surface area [22].

1.4 Neuroimaging and role of non-invasive methods in understanding glymphatics

To study CSF and ISF function and AQP4 contribution, different imaging techniques, such as *ex-vivo* and *in-vivo* fluorescence microscopy [8, 24] and *in-vivo* dynamic contrast-enhance (DCE) magnetic resonance imaging (MRI) [18, 25, 26], have been predominantly used in rodents [27]. These invasive techniques require injecting tracers into the brain cistern, that may alter the dynamics of the glymphatic system due to associated infusion artifacts [21, 26]. In addition, vast of the findings were reported based on *ex-vivo* assessment with microscopy imaging [28, 29, 30, 31]. These *ex-vivo* imaging have to be performed after applying perfusion-fixation and thus such approach produces profound changes in CSF flow direction and collapses the PVS, significantly altering the distribution of the trace as previously reported [32]. Therefore, the imaging with live animals is the current mainstream for glymphatic analysis

One of the current gold standard live imaging methods for glymphatic analysis is DCE-MRI. DCE-MRI requires tracer injection, typically gadolinium (Gd) -based contrast agents, into the brain cistern. When we inject Gd-based contrast agent into the brain cistern, Gd travels along the CSF space and some Gd infiltrate into the brain. T1-weighted imaging can depict the distribution of Gd as bright signal, therefore allowing to estimate how much tracer can travel from CSF to the brain. It is a powerful tool to study the glymphatic function, however, one considerably big drawback is its potential risk of deposition in the brain [33]. This risk might hinder the real fluid behavior in the brain parenchyma. To answer how AQP4 facilitates the glymphatic kinetics - especially among parenchymal regions of the brain-, a fully non-invasive assessment of the brain's water content and water molecules mobility in live animals is desired. Among many methods considered as state-of-the-art for neuroimaging [34], diffusion-weighted imaging (DWI) may provide information on random velocity and displacement of water molecules within the tissue [35, 36]. DWI measures the signal attenuation due to diffusion gradients, providing more functional than morphological assessment. Hence, it is primarily used for neuroradiological assessment in both preclinical and clinical studies [37, 38], including ischemic stroke [39, 40]. DWI provides a measurement of the tissue's diffusivity as a biomarker of pathological conditions. To date, some studies have shown the potential use of DWI as a non-invasive method to study the glymphatic system [41, 42, 43]. However, they have not well depicted the AQP4 specific function yet, and further technical improvement is necessary to answer the essential question how AQP4 facilitates the glymphatic system.

Another approach, providing more morphological evaluation, would base

on steady-state techniques where the T1 magnetization is constant across the whole acquisition [44]. As the aim of the current work is to validate a magnetic resonance (MR) protocol for the mouse brain water mobility and content, an application of T2-weighted imaging would be of use for assessing the brain CSF content as CSF would be clearly differentiable from surrounding parenchyma with high signal intensity. Still, further assessment of microscopic changes in ISF among different brain regions could encompass Dixon technique [45] at employed ultra-high field MRI. This way, an indirect assessment of the brain water content could be achieved using a gradient-recalled echo (GRE) sequence [46]. Thus, Dixon technique shall provide information on rather static components of the brain fat/water content for analyzed fully non-invasive glymphatic MRI approach.

1.5 Impact of noninvasive acquisition on the glymphatic studies

Current work focused on analysis of DWI images acquired using echo-planar imaging (EPI) sequence. With this abundant information, the analysis comprises a region-wise assessment of the diffusion parameters from two computational models: monoexponential apparent diffusion coefficient (ADC) (see section 3.2.1) and bi-exponential intravoxel-incoherent motion (IVIM) models (see section 3.2.1). Furthermore, acquired Dixon images were analyzed for various preprocessing assumptions to optimize for glymphatic assessments (see section 3.2.2). Dixon result is also validated in three different phantoms of the authors' own design. Dixon algorithm was applied to the images from 6-echoes GRE sequence (here multiple gradient-echo, MGE), as in *in-vivo* imaging, and additionally to the first four echoes and the last four echoes of the 6-echoes GRE acquisition. In addition, a rapid acquisition with relaxation enhancement (RARE) variable repetition time (VTR) and multi-slice multi-echo (MSME) sequences were employed to characterize the phantoms T1 and T2 relaxation times, respectively in every phantom.

1.6 Aims and summary of current work

The aim of this project was two-fold: analyze and validate a dedicated protocol for fully non-invasive glymphatic imaging at 9.4 T , based on DWI-EPI and GRE methods; by means of the protocol, provide sufficient estimates on free water mobility and content in AQP4 KO and WT animals.

Herein, the project aimed to analyze the data acquired *in-vivo* and further recalculated MR diffusion images in order to find specific differences in diffusion parameter between two animal genotypes, as well as to compare the findings between those from diffusion imaging with two different echo times: 22 ms , used as close to widely employed predominantly, and 30 ms as theoretically lowering the proton density signal contribution. Therefore, a larger applicability of higher echo time DWI specifically for the glymphatic imaging was confirmed (see chapter 4.1).

To further bring closer an idea of fully non-invasive glymphatic protocol, I performed calculation of Dixon fat and water maps using provided images. The images consisted of 6-echoes MGE, and calculation was performed using 4 different assumption of fat/water brain compositions (see chapter 3.2.2). The results obtained using a dedicated IDEAL algorithm [47, 48] were further validated by measurements in phantoms of the author's own design.

Hence, to bring closer the theoretical assumptions of my work, in the following section I aim to explain the background of MR techniques applied. This would make the respected reader understand the different MRI sequences applied during the project, before the methods for my work would be described. The following chapter of the text is based on the book MRI: the basics [49] and relevant papers explaining DWI [50, 51] and Dixon technique [52].

2 Theoretical background for MR imaging

2.1 Proton relaxation times

2.1.1 T1 relaxation time

T1 relaxation time is a fixed parameter at a given magnetic field strength for a given tissue.

In this text, the coordinate system used is shown in Figure 3.

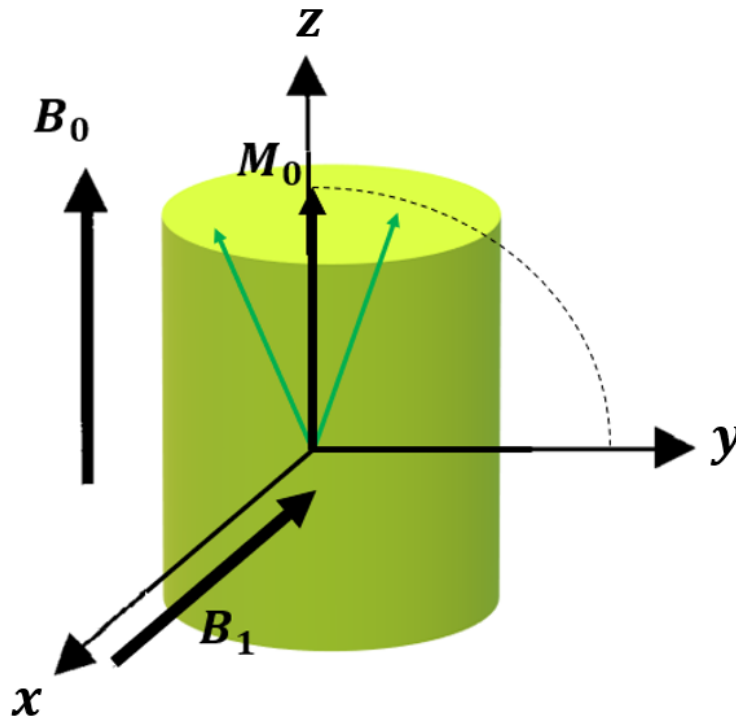


Figure 3: Coordinate system. An external magnetic field B_0 is applied along the z-axis, parallel to the longitudinal axis of the object imaged (green cylinder). The longitudinal magnetization, M_0 , sum of all the longitudinal magnetization of all the spins (light green arrows), is parallel to the B_0 axis. A radiofrequency (RF) pulse is applied perpendicular to B_0 and its magnetic field, B_1 , is parallel to the x-axis. A 90° RF pulse flips the net magnetization into the x-y plane (dashed arc).

In ideal conditions, in the presence of an external magnetic field, B_0 , parallel to the z-axis (see Figure 3), proton spins magnetization vectors (represented as light green arrows in Figure 3) will precess around B_0 at a frequency proportional to the external magnetic field strength, given by the Larmor equation:

$$\omega = \gamma \cdot B_0 \quad (1)$$

, where γ is the proton gyromagnetic ratio and B_0 is the strength of the external magnetic field. Therefore, the longitudinal magnetization of the proton spins precessing at $\omega_0 = \gamma \cdot B_0$ contribute to form a net magnetization parallel to the external magnetic field, called longitudinal magnetization M_0 . If a radiofrequency (RF) pulse perpendicular to the B_0 axis and with a magnetic field, B_1 , parallel to the x-axis (see Figure 3) is applied, the spins will precess around B_0 at the same time they precess around B_1 but at different frequencies, $\omega_0 = \gamma \cdot B_0$ and $\omega_1 = \gamma \cdot B_1$, respectively ($\omega_0 \gg \omega_1$). As a result, a 90° RF pulse flips the net magnetization into the orthogonal plane (x-y plane in Figure 3), represented by the dashed arc in Figure 3, obtaining a transverse magnetization M_{xy} .

Immediately after the 90° RF pulse, the magnetization M_{xy} precesses within the x-y plane, oscillating around the z-axis with all protons rotating in phase. When the RF pulse is turned off the spins 1) will go back to the lowest energy state and 2) will get out of phase with each other. These two processes occur independently. And as a result, the M_{xy} component of the magnetization vector decreases rapidly and the M_z component slowly recovers along the z-axis.

The rate at which M_z recovers its initial value, M_0 , is given by the longitudinal relaxation time or spin-lattice relaxation time, T1. The longitudinal magnetization M_z recovery is characterized by:

$$M_z = M_0 \cdot \left(1 - e^{-t/T1}\right) \quad (2)$$

The spin-lattice relaxation time refers to the time it takes to the spins to give away the energy received by the RF pulse to their lattice surroundings and recover their equilibrium state.

2.1.2 T2 relaxation time

After the 90° RF pulse has been applied and the magnetization vector was flipped to the orthogonal plane (i.e., x-y plane in Figure 3), the spins start to dephase and thus the transverse component of the magnetization will start to decay at a rate given by T2 and characterized by:

$$M_{xy} = M_0 \cdot e^{-t/T2} \quad (3)$$

There are two phenomena that will cause spins to dephase, 1) the spin-spin interaction in the lattice and 2) the external magnetic field inhomogeneities.

When spins are parallel to the external magnetic field they will create a slightly higher local magnetic field, whereas when spins are anti-parallel to the external magnetic field, they will create a slightly lower local magnetic field. Therefore, one spin local magnetic field will be affected by the spins next to it, making a difference in the overall homogeneity of the magnetic field to which the spins are exposed and thus their precessing frequencies. Therefore, the first cause of dephasing due to the spin-spin interactions is an inherent property of the tissue and is measured by the transverse relaxation time or spin-spin relaxation time T2. T2 relaxation time is also a tissue-specific parameter, fixed at a given magnetic field strength.

2.1.3 T2* relaxation time

The other cause of spins dephasing is the external magnetic field inhomogeneity. Slightly differences in the external magnetic field make spins precess at slightly different frequencies.

When the RF pulse is turned off, the signal received from the precessing spins will start to decay due to spin-spin interaction and the external magnetic field inhomogeneities. Therefore, the signal received by the coil (induced by the oscillating spins) called free induction decay (FID), would have an oscillatory component and an exponential decaying factor whose time constant is given by T2*: $e^{-t/T2^*}$.

Contrary to T2, T2* is not fixed for a specific tissue, since it depends not only on spin-spin interactions but on the external magnetic field inhomogeneities as well.

2.1.4 Gadolinium T1 and T2 shortening

The rare earth element gadolinium is the element with the greatest number of unpaired electrons, with 7 unpaired electrons, which make it a strong paramagnetic element. Paramagnetic substances become magnetized when they are in presence of an external magnetic field and their induced magnetization is in the same direction as the external magnetic field. Consequently, they increase the effective magnetic field causing T1 and T2 shortening on the tissues where they are present, although the predominant effect at low dose is T1 shortening [53].

2.2 MR sequences and signals

2.2.1 Spin-echo

In spin-echo (SE) sequences, the immediate effect of protons transverse magnetization vector dephasing (faster with increasing B_0) is removed by applying an additional 180° RF refocusing pulse a time τ after the 90° RF pulse. This makes spins to precess toward the opposite direction, and after an equal time τ from the 180° RF pulse the spins will get back to phase and the transverse magnetization will reach a maximum.

Therefore, the time 2τ is called the time to echo (TE) and it measures the time from the 90° RF pulse to the maximum of the rephased protons signal (the echo).

After a repetition time (TR), a new 90° RF pulse is applied, flipping again the longitudinal component of the magnetization to the orthogonal plane and the process is repeated.

Fast spin-echo

We can apply more than one refocusing pulse (multi-spin-echo) to acquire different echoes from the same 90° RF pulse, which is an extension of SE, providing acceleration of imaging using multislice or multiecho technique [54]. The different echoes will occur at different TEs from the 90° RF pulse. Still, the 180° RF refocusing pulse recovers only the part of the signal from the original FID that is due to external magnetic field and local inhomogeneities but not due to spin-spin interactions. Therefore, the maximum signal reached by consecutive echoes will be given by e^{-t/T^2} , where t corresponds to the different TEs from the different echoes, whereas the FID after the 90° RF pulse and after every echo is described by the constant $T2^*$.

2.2.2 Gradient-recalled echo

The major purpose of gradient-recalled echo is to significantly reduce the scan time. Long TRs are required in SE to recover enough longitudinal magnetization before the next 90° RF pulse, flipping the magnetization vector to the orthogonal plane, can be applied and in order to obtain a long enough transverse magnetization.

In GRE shorter TRs are possible because RF pulses yielding smaller excitation flip angles (α) are applied, instead of the 90° flip angle RF pulse applied in SE. Smaller flip angles produce incomplete flip of the longitudinal magnetization into the orthogonal plane, remaining most of the magnetization along the longitudinal axis. The magnitude of the transverse (M_{xy}) and longitudinal (M_z) magnetization are given by:

$$M_{xy} = M_0 \cdot \sin \alpha; \quad M_z = M_0 \cdot \cos \alpha \quad (4)$$

This remaining longitudinal magnetization allows applying shorter TRs and still having enough longitudinal magnetization to flip into the orthogonal plane (i.e., x-y plane; see Figure 3) with the next RF pulse.

One main difference between GRE and SE is that GRE does not allow for 180° refocusing pulses, and thus is not able to eliminate the dephasing caused by external magnetic field inhomogeneities. This 180° refocusing pulse is not possible in GRE because of the large longitudinal magnetization component at half the echo time that would be inverted pointing to the $-z$ direction. To recover this inverted magnetization back pointing to the $+z$ direction very long TRs would be necessary, which is not desirable in GRE.

Therefore, in GRE without 180° refocusing pulse no echo from the original FID is formed. To obtain the echoes, we need first to dephase the FID and then rephase (or recall) it again at the convenient time. This dephasing and rephasing steps are accomplished by bilobed gradients. This bilobed gradient has first one negative lobe that dephase the signal and then one positive lobe of the same absolute magnitude that the negative lobe but twice longer in time that initially rephase the signal obtaining an echo at the midpoint of the positive lobe (see Figure 4) and then it dephases it again.

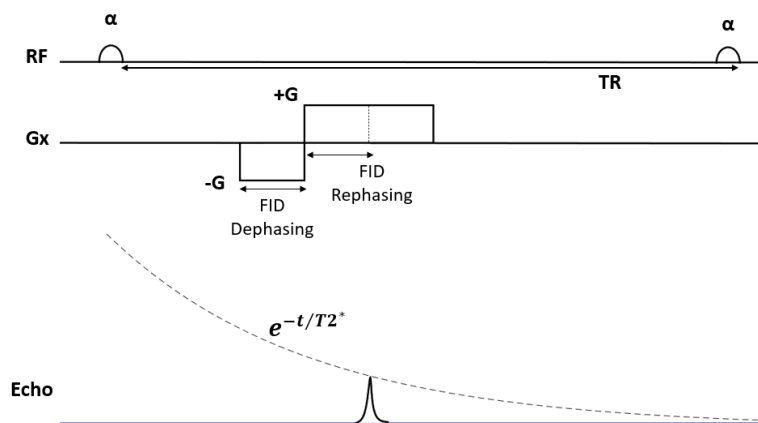


Figure 4: GRE diagram for RF pulse, the bilobed refocusing gradient and the echo. The bilobed gradient first dephases the FID and then it refocuses it, achieving the maximum at the midpoint of the positive lobe. The FID decay is governed by $T2^*$. This diagram is drawn based on the Figure 20-6 of 'MRI: the basics' [49].

In Figure 4 we can see a GRE diagram for the RF pulse, the bilobed refocusing gradient (applied along the x-axis) and the echo. The half circles

together with α represent the α flip angle RF excitation pulse. The second α RF excitation pulse is applied TR time after the first α RF excitation pulse. Since there is no 180° refocusing pulse that eliminate the dephasing due to external magnetic field inhomogeneities, the transverse magnetization maximums acquired at the following echoes decay at a rate given by $T2^*$.

The main advantage of GRE against SE is the increase of speed of acquisition allowing for 3D imaging in a reasonable scan time. However, the main disadvantages are a reduced signal-to-noise ratio (SNR) because of the small α flip angle, reducing the transverse magnetization. Furthermore, shortening of TR in case of large flip angle may not allow for sufficient longitudinal magnetization recovery. Another disadvantage is the signal decay governed by $T2^*$ instead of T2 because there is no 180° refocusing pulse, resulting in an increase sensitivity to the external magnetic field inhomogeneities and magnetic susceptibility artifacts [49]. In the end, SE provides so called 'true' tissue contrast, while GRE highly depends on stability of achieved T1 magnetization over the acquired image phase [44].

2.2.3 Multi-slice technique

SE sequences have long TRs that are necessary for enough longitudinal magnetization recovery. These TR times are much longer than the time required to perform all necessary steps (select a slice, phase-encode step and frequency encode) to finally obtain the echo signal (active time). For instance, TR may be around 1000 *ms* while the active time could be around 50 *ms*. There is a long 'dead time' between the echo acquisition of one line in the data space and the next 90° RF pulse for the next line in the data space. This 'dead time' can be used to scan other slices by applying a different 90° RF pulse with identical transmit bandwidth as the one used for the first slice but centred at a higher or lower Larmor frequency. For example, in Figure 5 the 'dead time' is used to scan two additional slices. After the signal from the first slice is acquired, another 90° RF pulse centred at a different Larmor frequency is applied to acquire the signal from a second slice. The sequence from the first slice is repeated and if there is enough time, additional slices can be scanned. The same phase-encoding gradient (G_y) is applied to obtain the same amount of dephasing in all the slices. The echoes from the different slices are sampled by the same frequency-encoding gradient.

To choose the different slices the same slice-selection magnetic gradient (G_z) is applied with the same bandwidth but centred at a lower or higher frequency to flip the protons 90° in a different slice.

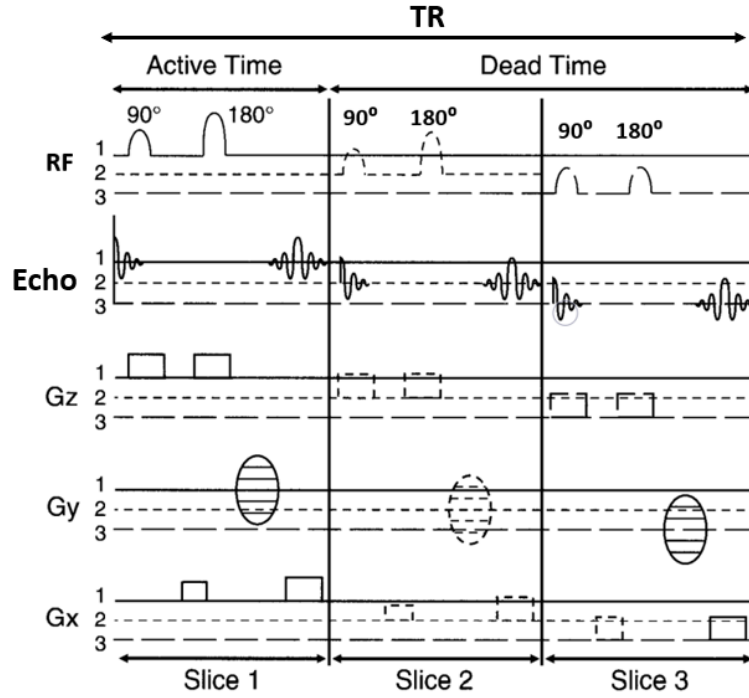


Figure 5: Multi-slice acquisition. The figure shows the SE pulse sequence diagram to scan three slices during the same TR, using the 'dead time' from the first slice acquisition. This figure is based on the Figure 12-7 of MRI: the basics [49].

2.2.4 Comparison SE vs. GRE

As a brief summary, I compare in table 1 the main characteristics in SE and GRE sequences.

Table 1: Comparison between SE and GRE main characteristics. NA – number of image averages, SNR – signal-to-noise ratio, N_y – number of rows in the data space, N_z – number of 'slices' in the data space when scanning in 3D, TR – time to repetition, RF – radiofrequency pulse, GRE – gradient-recalled echo, SE – spin-echo.

	SE	GRE
RF flip angle	90°	Low flip angle
180° refocusing pulse	Yes	No
TR	Long TR	Short TR
Number of phase encoding steps	N_y	
Scan time	$TR \times N_y \times NA \times \text{number of slices}$	
Scan time (3D)	$TR \times N_y \times N_z \times NA \times \text{number of slices}$	
SNR	> SNR(GRE)	< SNR(SE)

A few comments can be made from the characteristics summarized in Table 1.

Low flip angles in GRE allow for shorter TR, decreasing the scan time. Long TR times in SE present 'dead times' that can be used to scan multiple slices in the same TR. The number of slices that can be scanned in the same TR is $\leq TR/TE$. If all slices can be scanned in the same TR, the acquisition time is reduced to:

$$scan\ time(SE) = TR \cdot N_y \cdot NA \quad (5)$$

, where NA is the number of image averages, a higher NA increases the signal-to-noise ratio (SNR) of the image.

The lack of a 180° refocusing pulse in GRE makes the transverse magnetization decay at a rate given by $1/T2^*$. This result in higher sensitivity to magnetic field inhomogeneities, intravoxel dephasing and magnetic susceptibility artifacts.

The SNR in GRE technique is decreased per echo compared to the SNR in SE. This is because of a low flip angle that provides short transverse magnetization and short TR that doesn't allow for enough longitudinal magnetization recovery. However, more echoes are obtained in a shorter time, which can compensate for the former effect.

2.2.5 Echo-planar Imaging

In general for majority of MR sequences, in order to spatially locate where the signal that we receive comes from, we need to apply frequency- and phase-encoding gradients along the read (i.e., x-axis) and phase (i.e., y-axis) directions, respectively. This would be in addition to the slice-selective gradient, applied along the z-axis, the same direction of the external magnetic field. Here, the frequency-encoding gradient is applied during the time at which the echo is received, that is during readout. Hence, it assigns a different frequency to every column in which the data space is divided into (N_x columns in total). In SE and GRE, a different magnitude phase-encoding gradient needs to be applied for every row that the data space is divided into, N_y different rows, meaning N_y different phase-encoding steps. At each phase-encoding step, each row has a unique phase shift caused by the gradient. Furthermore, only one phase-encoding step is applied in one TR. In Figure 6A a SE pulse sequence diagram is shown. The G_z represents the slice selection gradient applied along the z-axis during the 90° RF and the 180° refocusing pulses. The G_x is the readout gradient, applied at the time the echo is received. The first G_x gradient is used for offsetting any phase

shift induced during frequency readout. G_y represents the different phase-encoding steps applied at each TR. Each phase-encoding step has a different gradient strength. This phase-encoding gradient can be applied between the 90° and 180° pulses or between the 180° pulse and the echo.

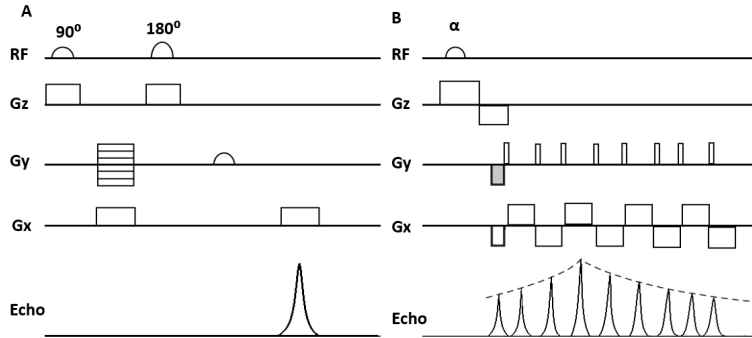


Figure 6: Panel A is a SE pulse sequence diagram. Each row in the data space is acquired after a different 90° RF pulse every TR. The readout gradient (G_x) is applied at the time that the echo is acquired. For every row acquisition, a different strength phase-encoding gradient (G_y) is applied. Panel B represents an echo-planar imaging (EPI) pulse sequence diagram. All rows from the data space are acquired after the same 90° RF pulse, during a single T2 or T2* decay. The phase-encoding gradient is briefly applied only while G_x is zero. This scheme is based on the Figures 11-9 and 22-3 of MRI: the basics [49].

Compared to both described SE and GRE, echo-planar imaging (EPI) allows for much faster acquisition of signals after RF pulse [55]. This is because EPI allows performing all phase-encoding steps in the same acquisition, after the same RF pulse (see Figure 6B). The frequency-encoding gradient, G_x , must be reversed rapidly from maximum positive to maximum negative $N_y/2$ times during a single T2* or T2 decay to acquire the different echoes. Each positive or negative lobe corresponds to a separate row in the data space. The phase-encoding gradient, G_y , is briefly applied N_y times while the readout gradient is zero, between each consecutive positive and negative lobe. In Figure 6B the decaying signal starts lower peaking afterwards because of the initial phase offset (G_y) (shaded area).

The main advantage of EPI is the short scan time, allowing to study the organ functions rather the organ anatomy. For instance, DWI can be performed by means of an SE-EPI sequence and application of diffusion gradients for better visualization of morphology compared to EPI. The consequence, however, is much longer acquisition time.

2.2.6 DWI

Still, fast imaging is required for measuring discrete biological process. DWI itself is based on microscopic particles fluid random motion, called Brownian motion. The Brownian motion of all the molecules in a fluid is responsible for the molecular diffusion. The distance reached by the molecules by means of diffusion is proportional to the diffusion time and the diffusion coefficient. When the molecules do not move freely but are constrained to some space, like inside the cell, the movement is restricted and an apparent diffusion coefficient (ADC) [50] measured using DWI is small as it is a function of the diffusion time, the geometry and the limiting volume in a voxel.

Diffusion movements in the presence of magnetic field gradients decrease the magnetic signal intensity. This decrease is due to the random phase shift produced by random displacements of the proton spins. The signal attenuation depends on the gradients strength, the diffusion coefficient and the diffusion time. In the case of a constant linear gradient of strength G and diffusion time TE , the signal amplitude of the n -th echo in a SE sequence is given by [50]:

$$\frac{S(n \cdot TE)}{S(0)} = \exp[(-n \cdot TE) / T2] \cdot \exp [(-\gamma^2 \cdot G^2 \cdot D \cdot n \cdot TE^3) / 12] \quad (6)$$

, where γ is the proton gyromagnetic ratio.

This signal attenuation due to restricted water molecules free mobility under the presence of gradients (slice-selection, readout phase-encode gradients plus additional gradients) can be used to determine the diffusion coefficient D . For this purpose, twin SE sequence [50] are used. These sequences have the same proton density and T1 and T2 relaxation components, but they differ on their response to incoherent motions in a voxel.

In the case where the molecules diffusion is constraint, the measured diffusion coefficient would be the apparent diffusion coefficient [50] (see section 3.2.1).

DWI signal is also affected by intravoxel incoherent fluid movements (IVIM), especially at low b values. Therefore, an application of bi-exponential IVIM model was considered to separate the ‘pure’ water diffusion from the pseudoperfusion water movements: [51, 56]

$$S(b) = S(0) \cdot \left(F_p \cdot e^{-b \cdot D^*} + (1 - F_p) \cdot e^{-b \cdot D} \right) \quad (7)$$

, where F_p is the perfusion fraction, D is the diffusion coefficient of ‘pure’ molecular water diffusion and D^* the pseudodiffusion coefficient.

Within the brain parenchyma, the psudoperfusion water motion is affected by perfusion in the microcirculation [57, 58, 59].

2.3 Dixon method

2.3.1 Basis

Magnetic resonance signals usually contain contribution from fat and water protons, resonating at slightly different frequencies [60]. In some cases, it is convenient to suppress the signal from fat because it appears hyperintense and it is often the water signal that is of primary interest.

There are some approaches that achieve fat suppression, such as chemical shift selective saturation [61], in which the fat magnetization is selectively excited and then saturated before imaging. Other approach employs a frequency selective RF pulse to only excite the water magnetization. However, both techniques are highly dependent on the external magnetic field homogeneity.

Another approach is Dixon technique [52] that can be used for computational separation of fat and water MR signals. As a result, a quantification of tissue fat or water content can be numerically obtained, by computing water-only and fat-only images.

Dixon technique relies on the water/fat chemical shift difference, σ . Water and fat protons have a slightly different Larmor frequency, meaning fat protons precess at slowly lower frequency than water protons. This frequency difference depends on the external magnetic field, B_0 , and it is given by:

$$\Delta f = \gamma \cdot \sigma \cdot B_0 \quad (8)$$

, where γ is the proton gyromagnetic ratio, σ is the chemical shift of fat relative to water and B_0 is the strength of the external magnetic field.

Original Dixon technique acquires an image with water and fat signals in-phase and another image with water and fat signals in opposing phase. Theoretically, by summation and subtraction of the two images we can obtain a water-only image and a fat-only image. Still, this is valid only in the ideal conditions, which in presence both B_0 and transmit RF-field inhomogeneities make the computation more complex [52, 62].

2.3.2 Signal modelling

Under the assumption that water and fat are the only chemical species imaged, the received complex signal can be expressed as follows:

$$S(x, y) = [W(x, y) + F(x, y) \cdot e^{i\alpha}] \cdot e^{i\phi(x, y)} \cdot e^{i\phi_0(x, y)} \quad (9)$$

, where (x, y) represents the pixel spatial coordinates, W and F are the magnitude of the magnetizations at a given pixel for water and fat, respectively, at the sampling time. α is the fat phase difference relative to water due to chemical shift difference, ϕ is the phase due to magnetic field inhomogeneities and ϕ_0 is the phase due to other system imperfections.

By controlling the time at which the signal is acquired we can obtain any phase shift, α , between the fat and the water signals:

$$\alpha = \gamma \cdot B_0 \cdot \sigma \cdot \Delta t \quad (10)$$

, where γ is the proton gyromagnetic ratio, σ is the chemical shift of fat relative to water and B_0 is the external magnetic field. Δt represents changes in echo time or time shifts from a spin echo.

The error phase ϕ due to the external magnetic field inhomogeneities also depends on Δt and is given by:

$$\phi = \gamma \cdot \Delta B_0 \cdot \Delta t \quad (11)$$

, where ΔB_0 represents the magnitude of the magnetic field inhomogeneities.

Magnitudes W , F , ϕ , ϕ_0 and ΔB_0 are spatially dependent and may vary from pixel to pixel. However, α , only depends on Δt and the chemical shift, and thus it is spatially independent and can be considered a constant.

This model assumes that water and fat only have one single spectral peak. While this is generally true for water, it has been shown that fat contain many spectral peaks [63]. The main contribution to the fat spectrum is a broad peak whose resonance frequencies are around 3.5 ppm ($\sigma = 3.5$ ppm) away from the water resonance frequency. However, there is another important contribution to the fat spectrum from the olefinic proton whose resonance frequency is around 0.5 ppm, which is very close to the water resonance frequency. That is why, in this model, even pixels containing only fat tissues may have signal contribution to both the water-only and the fat-only image.

As a convention, a Dixon technique that acquires two images for obtaining the only water and only fat images after postprocessing is called two-point Dixon technique. If three images are acquired then the technique is called

three-point Dixon. If 4 or 6 acquired images are used for the postprocessing, then it'll be a 4-point or 6-point Dixon technique, respectively.

2.3.3 Two-point Dixon

The original Dixon technique acquires one image where water and fat signals are in-phase ($\alpha = 0$), and another image where water and fat signals are 180° out-of-phase to obtain a water-only and fat-only image.

The signals received from the two acquisitions are described as follows:

$$\begin{aligned}\alpha = 0 &\longrightarrow S_0 = (W + F) \cdot e^{i\phi_0} \\ \alpha = 180^\circ &\longrightarrow S_1 = (W - F) \cdot e^{i\phi} \cdot e^{i\phi_0}\end{aligned}\tag{12}$$

When $\phi = 0$, that is $\Delta B_0 = 0$, there is no magnetic field inhomogeneities, W and F can be directly determined by:

$$\begin{aligned}W &= 0.5 \cdot |S_0 + S_1| \\ F &= 0.5 \cdot |S_0 - S_1|\end{aligned}\tag{13}$$

When ϕ is not zero, Dixon proposed to take the magnitude values $|S_0|$ and $|S_1|$ before summation and subtraction to separate the water and fat signals as follows:

$$\begin{aligned}W &= 0.5 \cdot (|S_0| + |S_1|) \\ F &= 0.5 \cdot (|S_0| - |S_1|)\end{aligned}\tag{14}$$

However, it can be seen that the obtained water-only image would be an image where every pixel contains the dominant signal (from the main specie in the pixel, that can be either water or fat) of the corresponding pixel. And the fat-only image would be an image where every pixel contains the least dominant signal of the corresponding pixel.

Therefore, even though the two-point Dixon technique correctly separates the signal from water from the signal from fat without knowing the phase error $\phi(x, y)$, the problem comes when making the correct binary choice on whether the summed or the subtracted result corresponds to the water or fat on a pixel level.

2.3.4 Three-point Dixon

By acquiring a supplementary image, additional information on the phase error ϕ can be calculated. Hence both W and F can be calculated using summation and subtraction. The third image can refer to the phase $\alpha = -180^\circ$ or at $\alpha = 360^\circ$. In the latter case, water and fat are potentially in-phase back again and the corresponding image can be characterized as:

$$\alpha = 360^\circ \longrightarrow S_2 = (W + F) \cdot e^{i2\phi} \cdot e^{i\phi_0} \quad (15)$$

From equations 12 and 15, the phase error ϕ can be calculated as:

$$\hat{\phi} = 0.5 \cdot \arg \{S_2 \cdot S_0^*\} \quad (16)$$

, where S_0^* is the conjugate complex of S_0 . If ϕ is correctly determined (i.e., $\phi = \hat{\phi}$), then the W and F images can be calculated as:

$$\begin{aligned} W &= 0.5 \cdot \left| S_0 + S_1 \cdot e^{-i\hat{\phi}} \right| \\ F &= 0.5 \cdot \left| S_0 - S_1 \cdot e^{-i\hat{\phi}} \right| \end{aligned} \quad (17)$$

The main issue with three-point Dixon imaging is the phase wrapping. For instance, if the calculated phase is shifted by 2π from the true phase, then $\hat{\phi}$ will differ from ϕ by π (because of the 0.5 in equation 16) which in turn will result in multiplying by a factor -1 the complex numbers in equations 17 and the solution of W and F will thus be interchanged.

If we don't know where phase wrapping has occurred, we have the same ambiguity as in the binary choice in the two-point Dixon technique. To solve this problem we must either require that no phase wrapping occurs or to find and correct the phase wrapping to obtain the true underlying phase.

By equation 11, requiring that no phase wrapping occurs is equivalent to require small external magnetic field inhomogeneities, which is the same requirement as that for the successful fat suppression by the frequency selective methods.

2.3.5 Phase unwrapping

Since the original Dixon technique, many algorithms have been developed to find and correct the phase wrapping and thus, obtain the true phase ϕ from its principal or wrapped value $\hat{\phi}$:

$$\phi = \hat{\phi} + k \cdot 2\pi \quad (18)$$

When phase wrapping occurs and multiples of 2π are added or subtracted, discontinuities between adjacent pixels appear. Phase unwrapping methods rely on the assumption that the true underlying phase ϕ is spatially smoothed or continuous. Phase unwrapping methods such as minimum-norm and the path following methods have been successfully used in Dixon imaging [52].

3 Methods

The analysis based on the *in-vivo* diffusion-weighted imaging (DWI) and multiecho Dixon MR images shared as initially acquired in the MRI Core Facility, Copenhagen University. All shared *in-vivo* images were subjected to motion-correction, and DWI images were recalculated using ADC and intravoxel incoherent motion (IVIM) models described in the chapter 3.2 of current manuscript. The multiecho images were motion-corrected, and the calculation of Dixon fat-only and water-only images was performed using the protocol described in the chapter 3.2.2. Further validation in the phantoms of authorship design, in images further acquired using the protocol from *in-vivo* scans (see section 3.3).

3.1 In-vivo imaging

All shared *in-vivo* images subjected to analysis were acquired, in 9 AQP4 knock-out (KO) and 9 wild-type (WT) littermate mice of 10-15 weeks age (56% females, *mean* \pm *standard deviation* (*SD*) 11.28 ± 1.45 weeks age, 23.61 ± 3.39 g body weight). No statistical difference in age and body weight were found between KO and WT (Figure 7).

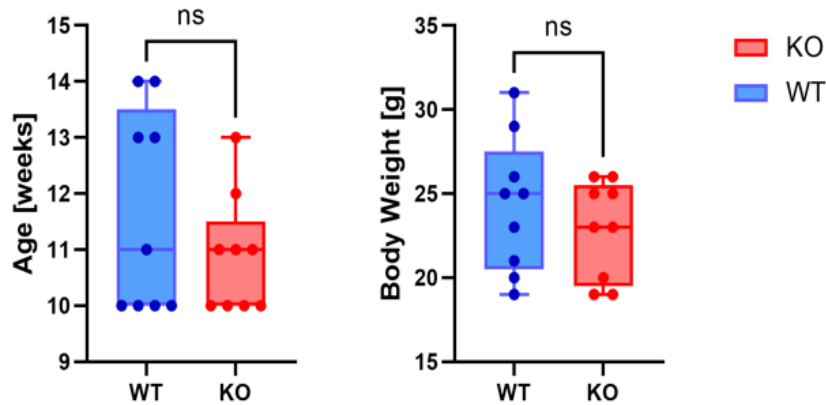


Figure 7: Whiskers-box plots for age (left) and body weight (right) distribution from 9 AQP4 KO and 9 WT littermate mice subjected to MR imaging.

In the original protocol all animals underwent 1H -MRI at 9.4 Tesla (BioSpec 94/30USR; 1500 *mT/m* BFG6S gradient coil; Bruker) using a volumetric transmit/receive resonator ($ID = 40$ mm), under general Ketamine/Xylazine anesthesia (K/X, 100/10 *mg/kg*).

The MRI protocol consisted of a respiratory-gated single-shot echo-planar DW imaging (2D-EPI-DWI) with 17 b-values ($0 - 2000 \text{ s}^2/\text{mm}$) measured in 3 orthogonal directions, and rf-spoiled gradient-recalled echo (GRE) acquired with 6 consecutive echoes for Dixon (2D-GRE; see Table 2). Overall, DWI at 22 and 30 ms TE was performed in 6 KOs and 6 WTs, and GRE in 9 KOs and 7 WTs. Complete DWI/Dixon MRI protocol was performed in 6 KOs and 4 WTs due to time constraints connected with anesthesia and associated scanning.

Table 2: *In-vivo* imaging scanning parameters. Legend: TR – time to repetition; TE - time to echo; FA – flip angle; FOV – field of view; TA–time of acquisition (Maximal time including pre-scan MR adjustments); EPI- echo-planar imaging sequence;

Sequence (Orientation, position)	2D-EPI (coronal, prone)	2D-GRE
Purpose	DWI	Dixon
TR [ms]	3570/3500	750
TE [ms]	22/30	2.19, 2.99, 3.79, 4.60, 5.41, 6.22
FA [deg]	90	10
FOV [mm ³]	16.2 × 14.4 × 11.2	16 × 16 × (9.8-11.2)
Averages	3-6	3
Voxel size [mm ³] (interpolation)	0.15 × 0.15 × 0.5 (0.2 mm gap, 16 slices)	0.125 × 0.125 × 0.5 (0.2 mm gap, 14 – 16 slices)
Bandwidth [Hz/pixel]	3307	1478
TA	< 45 min	

3.2 In-vivo images analysis

DWI was employed to find significant difference in the diffusion parameters between KO and WT. And Dixon imaging was used to analyse the differences in water fraction in the mice brain between the KO and WT groups.

To reduce the influence of frame-to-frame displacement during MRI, all DWI and Dixon (GRE) images from every subject underwent rigid-body motion correction. Afterward, DWI images were averaged from all directions and intensity-normalized volume-wise to the mean value of the background noise defined as a circular region outside the brain image of every animal, for further ADC and IVIM-DWI maps calculation.

Analysed 2D-EPI DW images were obtained in $n = 12$ subjects (6 WT

and 6 KO) at two different TEs, i.e. at 22 and 30 *ms* and without a change in the rest of the parameters (see Table 2). In the first instance, the shortest achievable TE of 22 *ms* was applied. In the second acquisition, a longer time of 30 *ms* was used to reduce the influence of high intensity ghosting, proton density or residual from physiological pulsations on DWI. Both acquisitions were acquired in the respiratory-gating mode to reduce the effects of the breathing [64] on estimation of water diffusivity, and the signal saturation bands were applied at the level of the cervical spine and the ventral head area to reduce the effects of arterial pulsations and motion on the DWI results. Slight difference in the time to repetition (TR) times (3500 vs 3570 *ms*) applied in both acquisitions is considered as negligible as allows full T1 recovery for the applied flip angle (FA) in both acquisition (FA of 90°, TR times > 3 × mean T1 for the brain parenchyma). Finally the ADC and IVIM-DWI models were applied for calculation of MR diffusion parameters.

3.2.1 Theoretical perspective of DWI images calculation

From the theoretical perspective, the calculation of ADC maps from DWI images was introduced by Le Bihan [50], and considers a mono-exponential decay behavior, ADC model, of the signal intensity with increasing b-values:

$$S(b) = S(0) \cdot e^{-b \cdot ADC} \quad (19)$$

, where $S(b)$ represents the mean signal intensity from the DWI image acquired at the b-value b , $S(0)$ is the signal intensity at $b = 0 \text{ s/mm}^2$, and ADC is the apparent diffusion coefficient.

From a set of 17 DWI images coming from different b-values each, for every animal, average ADC and S_0 (estimated image without diffusion weighting) maps were calculated voxel-wise based on the equation 19.

IVIM model [51], on the other hand, is an extension of the ADC model assuming presence of at least two components forming the DW signal: slow and fast diffusion. Therefore, a standard DWI signal is modelled by a bi-exponential curve to separate diffusion (D) from pseudodiffusion effects (D^*):

$$S(b) = S(0) \cdot (F_p \cdot e^{-b \cdot D^*}) + (1 - F_p) \cdot e^{-b \cdot D} \quad (20)$$

, where F_p is the perfusion fraction, D is the diffusion coefficient of ‘pure’ molecular water diffusion and D^* the pseudodiffusion coefficient.

For IVIM-DWI, a two-step algorithm [65] was used as considered providing more robust and reliable results compared to standard bi-exponential curve-fitting (equation 20). The IVIM threshold was set to a measured

230 s^2/mm b-value.

To perform further analysis, I was provided the motion corrected DWI images together with the fitted parameters maps from the ADC and IVIM models.

3.2.2 Dixon calculation

Dixon images were obtained in $n = 16$ animals (9 KOs and 7 WTs). From the motion-corrected multiple gradient-echo (MGE) (6-echoes GRE) images based on [66], I calculated the water-only and fat-only images by means of the Hierarchical IDEAL algorithm [47, 48] using the Fat-Water Toolbox [67] assuming the presence of 0, 1, 2 and 6 fatty acids double bonds.

The assumption of 0, 1 and 2 fatty acids double-bonds was made based on previous report [68], that fatty acids with 0, 1 and 2 fatty acids double bonds may account for $\approx 97\% - 98\%$ of total fat in humans on ordinary Western diet [68], and total polyunsaturated fatty acids composition in the brain is low and variable based on pathophysiological conditions [69]. 6 fatty acids double bonds assumption represent a border criteria, where the algorithm was tested for sensitivity in separation of fat and water signals in theoretically not physiological conditions or in the presence of image artifacts limiting separation of the signal [70].

Before calculating the water and fat fraction (WF and FF) maps, all voxel intensities < 0 were set to zero. The WF and FF maps were obtained subject-wise by voxel-wise comparing the intensities from the water and fat, respectively, to the sum of intensities from the fat and water images, as:

$$\begin{aligned} WF &= \frac{\textit{water intensity value}}{\textit{water intensity value} + \textit{fat intensity value}} \\ FF &= \frac{\textit{fat intensity value}}{\textit{water intensity value} + \textit{fat intensity value}} \end{aligned} \quad (21)$$

3.2.3 DWI and Dixon ROI setting

From the motion-corrected DWI images 12 brain regions of interest (ROIs) (see table 3) were manually set in [ITK-SNAP](#) [71] based on the [Allen Mouse Brain Atlas](#) [72]. These ROIs served as masks to calculate the average of the diffusion parameters values of the voxels within every ROI. The mean values will characterize the different brain regions and will be used for further statistical analysis.

From the motion corrected Dixon images and for reference for further ROI setting, a multiple echo data image combination (MEDIC) was calculated animal-wise as a sum of all GRE images of different echo times. From the MEDIC images 19 brain ROIS (see table 3) were manually set in *ITK-SNAP* [71] based on the *Allen Mouse Brain Atlas* [72]. These ROIs served as masks to calculate the average of the WF and FF of the voxels within every ROI. The mean values characterize the different brain regions and were used for further statistical analysis.

Table 3: Brain ROIs set for Dixon and DWI analysis. Green color- region set in the corresponding technique. Red color- region not set in the corresponding technique

ROI	Dixon	DWI
Cingulate Area	Green	Green
Olfactory Area	Green	Green
Lateral Ventricle (LV)	Green	Green
Third Ventricle (3V)	Green	Green
Hippocampal Area	Green	Green
White Matter	Green	Red
Caudoputamen	Green	Green
Cortex (S1)	Green	Green
Cortex (V1)	Green	Green
Cortex (Aud)	Green	Green
Optic Nerve	Green	Red
Hypothalamus	Green	Green
Thalamus	Green	Green
Pallidum	Green	Red
Substantia Nigra	Green	Green
Retrosplenial Cortex	Green	Red
Midbrain	Green	Red
Hindbrain	Green	Red
Periaqueductal gray	Green	Red

3.3 Ex-vivo imaging

For validation of *in-vivo* findings using Dixon technique, different phantoms were built as own design, and scanned using 9.4 T MR systems. The phantoms were designed to mimic a tissue with known fat and water composition, allowing to verify the sensitivity of Dixon technique in separating the fat and water signals in the current study.

3.3.1 Water phantom with gadolinium contrast

The first phantom consisted of 4 different vials with artificial CSF (aCSF) with different gadobutrol concentrations, 0, 0.01, 0.001 and 0.0001 mM/mL . Gadobutrol (Gadovist™ (EU)/Gadavist® (USA)) is a gadolinium-based contrast agent. The four vials were included in a wider tube filled in with distilled water without Gd, to facilitate the shimming of the B_1 field. This phantom was designed to: 1) verify Dixon algorithm and validate the potential and action of the Dixon algorithm in depicting fat signal and other signal from the water solution; 2) to decide on the best gadolinium concentration allowing to achieve the optimal T1 shortening for the signal amplitude depicted using original MSME sequence (see Table 4), and for further application in the Dixon phantom design.

The MRI protocol for this phantom consisted of two-dimensional sequences: 1) two RARE sequences for B_1 inhomogeneity correction using double angle method [73, 74]; 2) a MSME sequence for T2 mapping; 3) RARE variable TR (RAREVTR) sequence for T1 mapping; 4) two-dimensional rf-spoiled GRE (2D-GRE) with 6 consecutive echo times (here multiple gradient-echo, MGE) for Dixon imaging (Bruker sequence: MGE – multiple gradient echo) (see in Table 4). Further calculated T1 and T2 maps were used to validate if the depicted signal in our MGE sequences optimally (close to the maximal enhancement) for the shortening of T1 given by Gd. The MRI protocol for the water phantom is shown in Table 4.

3.3.2 Dixon phantom with gadolinium contrast.

Fat/water-Dixon phantoms were built to examine the sensitivity of Dixon technique in depicting different, especially small, fat fractions between 2 and 10%, the most frequently encountered in mice of normal conditions [69].

The first fat-water phantom consisted of 7 different vials, two only water compartments, aCSF and aCSF with 0.001 mM/mL Gd (this concentration was decided based on the results from the only water phantom) and 5 different fat-water emulsions with 0%, 2%, 10%, 25% and 100% fat content solutions.

A picture of this phantom is shown in Figure 8.

The fat-water emulsions were built according to a modified protocol described by Bush et al. [75], by mixing different percentages of 3% agarose and peanut oil solution with surfactants at 300°C and 1100 *rpm*. The water solution is compound of 3 *g* of agarose, 0.1 *g* Sodium Benzoate and

Table 4: Details of the MR sequences employed for validation of the *in-vivo* Dixon imaging in the water phantom. Legend: TR – time to repetition; TE - time to echo; FA – flip angle; FOV – field of view; TA–time of acquisition; MSME – multi-slice multi-echo; MGE – multiple gradient-echo; RARE – rapid acquisition with relaxation enhancement; RAREVTR – RARE variable time to repetition; *14 TRs: 15000, 8000, 4000, 2000, 1000, 600, 400, 300, 200, 120, 100, 50, 20, 15 *ms*.

Sequence (orientation)	RARE (axial)	MSME (axial)	RAREVTR (axial)	MGE (axial)
Purpose	B_1 map	T_2 map	T_1 map	Dixon
TR [<i>ms</i>]	1000	2000	*14 TRs	750
TE /echo space [<i>ms</i>]	7.3/7.3	6.5/6.5 40 echoes	4.6/4.6	2.18/0.82 6 echoes
FA [<i>deg</i>]	90/45	90	90	10
FOV [mm^3]	$16.2 \times 16.2 \times 2.8$	$16.2 \times 16.2 \times 1.0$	$16.2 \times 16.2 \times 2.0$	$16.2 \times 14.4 \times 2.0$
Resolution [mm^3]	$0.1 \times 0.1 \times 0.1$ 0.2 <i>mm</i> gap 10 slices	$0.15 \times 0.15 \times 0.1$ no gap 1 slice	$0.15 \times 0.15 \times 2.0$ no gap 1 slice	$0.15 \times 0.15 \times 2.0$ no gap 1 slice
Averages	20	10	10	5
Bandwidth [<i>Hz/pixel</i>]	309	926	926	2205
TA	54 <i>min</i>	36 <i>min</i>	9 h 33 <i>min</i>	6 <i>min</i>

0.2 *mL* of Tween20 [Merck, Denmark] per 100 *mL* of distilled water with 0.001 *mM/mL* Gd and the oil solution is compound of 1.0 *mL* of Span80 [Merck, Denmark] per 100 *mL* of peanut oil. Agarose is a polysaccharide that was used as a gelling agent, Sodium Benzoate is an organic sodium salt with preservative function, Tween20 is a nonionic detergent and Span80 is a nonionic surfactant that are very effective at forming oil in water emulsions and that is why they are used as emulsifying agents.

Peanut oil was chosen to mimic the fat component in the phantom because its proton nuclear magnetic resonance spectrum is similar to that of triglyceride protons in adipose tissue [76]. The oil is comprised of approximately 9% palmitic (16 : 0), 4% stearic (18 : 0), 55% oleic (18 : 1), and 27% linoleic (18 : 2) acids [77]. Peanut oil is compounded by fatty acids with 0, 1 or 2 fatty acids double bonds with an average of 1.09 fatty acids double bonds per fatty acid in the oil.

Gadolinium was added to verify how much the paramagnetic contrast would shorten the protons relaxation, and potentially altering the computation of Dixon images. The MRI protocol for this phantom was the same as the one for the water phantom (see section 3.3.1, Table 4) but it also included

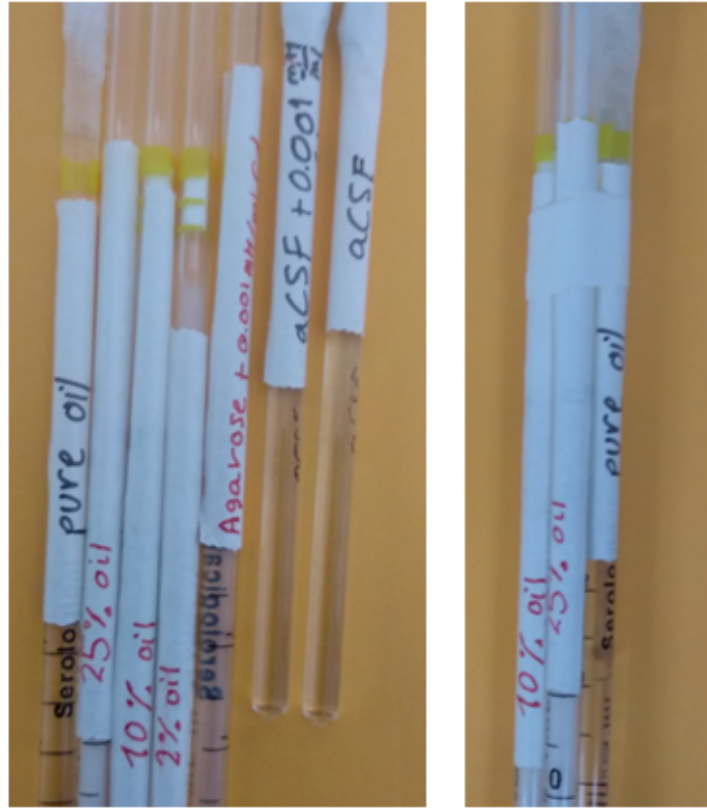


Figure 8: Dixon phantom with gadolinium. The phantom is formed by 7 compartments: aCSF, aCSF with 0.001 mM/mL Gd and 5 different fat-water emulsions with 0%, 2%, 10%, 25% and 100% fat solution.

2 RARE sequences with different inversion recovery (IR) times to measure the signal intensity cancellation of the main compartments. The RARE sequences were acquired at inversion-recovery times: 300 and 500 *ms*. The MRI protocol for the Dixon phantom with Gd contrast is shown in Table 5 and Table 6.

3.3.3 Dixon phantom without gadolinium contrast

To verify the performance of Dixon method and IDEAL algorithm in the presence of solutions without paramagnetic contrast agent (i.e. natural solutions), and to check whether the contrast agent might influence the results of Dixon method, an alternative phantom was designed.

The protocol used to make the fat and water emulsions was identical to the previous (see section 3.3.2), but in this case distilled water with no gadobutrol was used. Again, 7 vials with different fat content of 0%,

Table 5: Details of MR sequences employed for T1, T2 and B_1 mapping in the fat/water Dixon phantom with Gd. Legend: TR – time to repetition; TE - time to echo; FA – flip angle; FOV – field of view; TA–time of acquisition; MSME – multi-slice multi-echo; MGE – multiple gradient echo; RARE – rapid acquisition with relaxation enhancement; RAREVTR – RARE variable time to repetition; *8 TRs: 15000, 8000, 4000, 2000, 1000, 500, 200, 100 *ms*.

Sequence (orientation)	RARE (axial)	MSME (axial)	RAREVTR (axial)
Purpose	B_1 map	T_2 map	T_1 map
TR [<i>ms</i>]	1000	2000	*8 TRs
TE /echo space [<i>ms</i>]	6.0/6.0	6.55/6.55 40 echoes	6.0/6.0
FA [<i>deg</i>]	90/45	90	90
FOV [mm^3]	$16.2 \times 16.2 \times 3.0$	$16.2 \times 16.2 \times 3.0$	$16.2 \times 16.2 \times 3.0$
Resolution [mm^3]	$0.1 \times 0.1 \times 3.0$ no gap 1 slices	$0.1 \times 0.1 \times 3.0$ no gap 1 slice	$0.1 \times 0.1 \times 3.0$ no gap 1 slice
Averages	10	10	10
Bandwidth [<i>Hz/pixel</i>]	309	617	309
TA	27 <i>min</i>	54 <i>min</i>	1 h 24 <i>min</i>

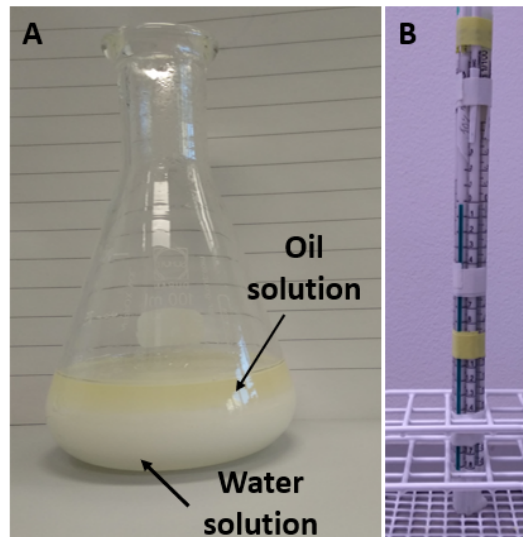


Figure 9: Panel A shows 50% fat content emulsion. The emulsion shows visible separation between the fat and water solutions. Panel B shows the Dixon phantom without Gd. The phantom is composed of 7 vials with different fat content of 0%, 2%, 10%, 25%, 50%, 50% and 100%.

Table 6: Details of MR sequences employed for Dixon imaging (MGE) along with verification of the prior estimated approximate fat and water solutions T1 times, using IR RARE sequence for the Dixon phantom with Gd. Legend: TR – time to repetition; TE - time to echo; FA – flip angle; FOV – field of view; TA–time of acquisition; *IR: Inversion recovery sequences were used to measure the signal intensity cancellation of the main compartments. The RARE sequences were acquired at IR times: 300 and 500 *ms*.

Sequence (orientation)	MGE (axial)	RARE (axial)
Purpose	Dixon	*IR IR times: 300 and 500 <i>ms</i>
TR [<i>ms</i>]	750	5000
TE /echo space [<i>ms</i>]	2.18/0.81 6 echoes	6.0/6.0
FA [<i>deg</i>]	10	90
FOV [<i>mm</i> ³]	16.2 × 16.2 × 3.0	16.2 × 16.2 × 3.0
Resolution [<i>mm</i> ³]	0.127 × 0.127 × 3.0 no gap, 1 slice	0.1 × 0.1 × 3.0 no gap, 1 slice
Averages	2	10
Bandwidth [<i>Hz/pixel</i>]	1860	309
TA	4 <i>min</i>	2 h 15 <i>min</i>

2%, 10%, 25%, 50%, 50% and 100% were included and tied together with nonmagnetic-tape. The 50% fat content emulsion showed a visible separation between the fat and water solutions (see Figure 9A). Therefore, two different 50% fat content vials were included for comparison, because of the great difficulty to emulsify high fat fraction solutions and to keep them consistent in small diameter pipettes used. The 100% fat content solution was solely compound of 1.0 *mL* of Span80 per 100 *mL* of peanut oil. The Dixon phantom without Gd is shown in Figure 9B.

The MRI protocol for this phantom was the same as the one for the water phantom (see section 3.3.1, Table 4) but it also included 2 RARE sequences with inversion-recovery pulses of 500 and 1500 *ms*.

The MRI protocol for the Dixon phantom without gadolinium is shown in Table 7 and Table 8.

Assuming a chemical shift of fat relative to water of $\sigma = 3.5$ *ppm*, the phantoms were scanned using GRE sequence for *in-vivo* imaging (here MGE)

Table 7: Details of MR sequences employed for T1, T2 and B_1 mapping in the fat/water Dixon phantom without Gd. TR – time to repetition; TE - time to echo; FA – flip angle; FOV – field of view; TA–time of acquisition; MSME – multi-slice multi-echo; RARE – rapid acquisition with relaxation enhancement; RAREVTR – RARE variable time to repetition; *14 TRs: 15000, 10000, 8000, 6000, 4000, 2000, 1000, 800, 500, 300, 100, 80, 60, 40 *ms*.

Sequence (orientation)	RARE (axial)	MSME (axial)	RAREVTR (axial)
Purpose	B_1 map	T_2 map	T_1 map
TR [<i>ms</i>]	2000	2000	*14 TRs
TE /echo space [<i>ms</i>]	6.0/6.05	6.55/6.55 80 echoes	6.0/6.05
FA [<i>deg</i>]	90/45	90	90
FOV [mm^3]	$19.2 \times 19.2 \times 3.0$	$19.2 \times 19.2 \times 3.0$	$19.2 \times 19.2 \times 3.0$
Resolution [mm^3]	$0.1 \times 0.1 \times 1.0$ no gap 3 slices	$0.1 \times 0.1 \times 1.0$ no gap 3 slice	$0.1 \times 0.1 \times 1.0$ no gap 3 slice
Averages	10	10	10
Bandwidth [<i>Hz/pixel</i>]	289	465	289
TA	1 h 4 min	1 h 4 min	12 h 47 min

(see Table 4), employing 6 consecutive echo times acquired at 2.18, 2.99, 3.8, 4.61, 5.42 and 6.23 *ms* with echo spacing of 0.81 *ms*, which is around 1.14 times the period at which water and fat protons are in-phase. The first echo image is acquired at in-phase, the second echo image is acquired at dephased in-phase, the third echo image is acquired in the middle of in- and opposed-phase, the fourth echo image is acquired at opposed-phase, the fifth echo image is acquired dephased opposed-phase and the sixth echo image is acquired in the middle of opposed- and in-phase. The echo space was chosen mainly because of the scanner minimum echo spacing limited due to the MR receiver bandwidth for the minimal optimal image resolution set.

3.4 Processing of the phantom images

All T1, T2 and Dixon images from every phantom underwent rigid-body motion correction performed in MANGO image analysis software [version 4.1, Research Imaging Institute, UTHSCSA], to reduce the frame-to-frame displacements of the acquired images. Still, it is worth to highlight, that no significant differences between the original and motion-corrected images was obtained so the whole further processing pipeline could be applied similarly to unprocessed images. T1 mapping was performed using VTR (see

Table 8: Details of MR sequences employed for Dixon imaging (MGE) along with verification of the prior estimated approximate fat and water solutions T1 times, using IR RARE sequence for the Dixon phantom without Gd. TR – time to repetition; TE - time to echo; FA – flip angle; FOV – field of view; TA–time of acquisition; MGE - Multiple gradient-echo; *IR: Inversion recovery sequences were acquired at IR times: 500 and 1500 *ms*.

Sequence (orientation)	MGE (axial)	RARE (axial)
Purpose	Dixon	*IR IR times: 500 and 1500 <i>ms</i>
TR [<i>ms</i>]	750	5000
TE /echo space [<i>ms</i>]	2.18/0.81 6 echoes	6.42/6.42
FA [<i>deg</i>]	10	90
FOV [<i>mm</i> ³]	19.2 × 19.2 × 3.0	19.2 × 19.2 × 3.0
Resolution [<i>mm</i> ³]	0.127 × 0.127 × 1.0 no gap 3 slice	0.1 × 0.1 × 1.0 no gap 3 slice
Averages	2	5
Bandwidth [<i>Hz/pixel</i>]	1840	261
TA	4 <i>min</i>	1 h 20 <i>min</i>

Tables 4, 5 and 7). Furthermore, RARE sequences using different inversion times were acquired to verify estimated T1 times in each phantom solution, based on the signal cancellation in both Dixon phantoms (with and without gadolinium). T2 mapping was performed using MSME sequence (see Tables 4, 5 and 7). Both T1 and T2 mapping would provide estimates on stability of the measurements, and aimed to confirm existence of differences in relaxation times between different phantom solutions. Further, such information would reflect possibility of depicting differences in fat/water composition using Dixon based on the steady-state GRE technique.

3.4.1 T1 mapping using RARE variable TR

Before fitting the RAREVTR images for the T1 mapping, the images were subjected to the mean background noise intensity subtraction frame-wise to automatically depict only the regions belonging to the phantom solutions. The noise region was manually defined in the image of every phantom, and composed of four different square ROIs 9 × 9 pixel each placed at the far corners of the images, outside the phantom position. Subsequently, the mean

and standard deviation of the noise ROI intensities were calculated, and their sum was subtracted voxel-wise from the first RARE image acquired with the longest TR. After subtraction, the voxels of intensity > 0 were included into the voxel-wise T1 fitting. This way, only the voxels belonging to the phantom image would be included in further T1 map calculation. The automatic mask calculation was performed in MATLAB [version 9.11.0 (R2021b), The Mathworks Inc., Natick Massachusetts].

Therefore, the mask consisted of circular regions covering the inner area of every vial image and excluding the vials' borders affected by a higher partial volume effect.

Subsequently, for every phantom mask voxel that were included in the T1 mapping, the signal intensities from all the RAREVTR images were fitted according to equation 22:

$$S = S_0 \cdot \left(1 - e^{-t/T1}\right) + \epsilon \quad (22)$$

, where S represents the image intensities over changing TR values, S_0 is the signal intensity acquired at infinite time (here the longest TR of 15 seconds, i.e. > 5 times the T1 of water at 9.4 T), T1 is the corresponding spin-lattice relaxation time of the solution and ϵ is additive noise. The fitting parameters are S_0 , T1 and ϵ .

To verify a proper calculation for the T1 maps, an IR RARE sequence was employed to measure the signal cancellation in the main vials consisting of 100% FF (pure oil) and between 10% and 25% FF (with and without gadolinium), by using the inversion time of 500 and 300 ms , respectively, for the Dixon phantom with gadolinium and 500 and 1500 ms , respectively, for the Dixon phantom without gadolinium.

3.4.2 Radiofrequency transmit field inhomogeneity correction (B_1^+ -correction)

Raw acquired T1 mapping was shown to provide high discrepancy between the estimates and real relaxation values [78]. To provide higher accuracy, a B_1^+ radio-frequency field inhomogeneity correction was performed voxel-wise for all the phantoms. To compare, the T1 maps were calculated before and after applying the B_1^+ inhomogeneity correction.

B_1^+ inhomogeneity maps (B_1^+ maps) were calculated from two spin-echo (here RARE) sequences using double angle method [73, 74] at two different excitation flip angles, at one nominal (set parameter during the scanner) flip

angle α and at 2α . We used $\alpha = 45^\circ$ and $2\alpha = 90^\circ$.

Due to magnetic field inhomogeneities, the effective excitation flip angle α_{eff} would slightly differ from the nominal α angle [79]:

$$\alpha_{eff} = B_1(x, y) \cdot \alpha \quad (23)$$

Therefore, B_1 correction map was calculated as follows [73]:

$$B_1 = \frac{\alpha_{eff}}{\alpha} = \frac{\arccos\left(\frac{S_2}{2S_1}\right)}{\alpha} \cdot \frac{180^\circ}{\pi} \quad (24)$$

, where S_2 and S_1 are the voxels intensities of the images obtained with 2α and α flip angles respectively. We can see that the B_1^+ -correction map is a relative and dimensionless map with numbers around 1, where a number below and above 1 in a pixel means an effective excitation flip angle higher and lower than the nominal excitation flip angle, respectively, in that voxel. And an exact value of 1 will mean that the effective flip angle is the nominal flip angle.

To obtain the T1 map after B_1 correction inhomogeneities we multiply the T1 map by the calculated B_1 correction map [80]:

$$T1_{corr} = T1 \cdot B_1 \quad (25)$$

, where $T1_{corr}$ and $T1$ are the corrected T1 map and T1 map respectively, and B_1 is the B_1^+ inhomogeneities correction map.

3.4.3 T2 mapping

To obtain the T2 maps, the background noise was subtracted image-wise from the MSME images, as the RAREVTR images were processed before T1 fitting. Moreover, distinguishable and well-delimited regions for T2 mapping were automatic depicted by setting an empirical signal intensity threshold.

For every pixel within the separated by the automatic mask calculation (see section 3.4.1) regions for T2 mapping, the signal intensities from the different TE's was fitted assuming an exponential decay behaviour typical of the FID plus an additive noise contribution:

$$S = S_0 \cdot e^{-t/T2} + \epsilon \quad (26)$$

, where S represents the image intensities over changing TE times at which the signal intensity was depicted. $T2$ is the transverse relaxation time constant for the type of tissue, S_0 is the signal intensity at exactly the time of

the echo ($t = 0$) and ϵ is the additive noise contribution. S_0 , $T2$ and ϵ are the fitting parameters.

3.4.4 Dixon images calculation

Dixon fat and water images were calculated from the 6 echoes GRE sequence (MGE adapted for 6-point Dixon), by means of the Hierarchical IDEAL algorithm [47, 48].

In-phase and opposed-phase images were considered as 1st and 4th echo images, respectively, while the sequence was adapted according to [81], where each consecutive echo was shifted approximately by $2\pi/3$, here we shifted 2.28π .

To verify the potential of the reduced number of acquired echo times on the fat-water separation using the algorithm, supplementary computations were performed considering only the images acquired with the first four echoes (2.2, 3.0, 3.8 and 4.6 *ms*) and the last four echoes (3.8, 4.6, 5.4 and 6.2 *ms*), i.e. 4-point Dixon. Such approach was chosen as the fat/water separation can potentially be affected by not fully achieved steady state in the first TE GRE image or too low SNR of the last GRE images acquired. Moreover, calculation using reduced number of TEs would bring the protocol closer to those used in the clinical scanners, where the time of acquisition and deposition of energy into the patient’s body are primary concerns.

Finally, all Dixon images were calculated assuming presence of 0, 1, 2 and 6 fatty acids double bonds, as previously described.

In addition, we verified the influence of the B_1^+ -correction on the results of the fat/water separation using IDEAL algorithm. Furthermore, we have checked the influence of gaussian smoothing on the Dixon results in both the original and the images after B_1^+ -field correction. Gaussian smoothing was performed in MANGO [version 4.1, Research Imaging Institute, UTHSCSA] using a 1σ Gaussian kernel.

From the motion-corrected images different circular-shaped ROIs, covering the inner part of the vials and excluding their borders because of higher partial volume, were manually set in ITK-SNAP [71] (see example in the Figure 10). The WF and FF of every pixel within these ROIs were calculated comparing voxel-wise the intensities from the water-only image and the fat-only image, respectively, to the sum of the intensities of the water and fat images.

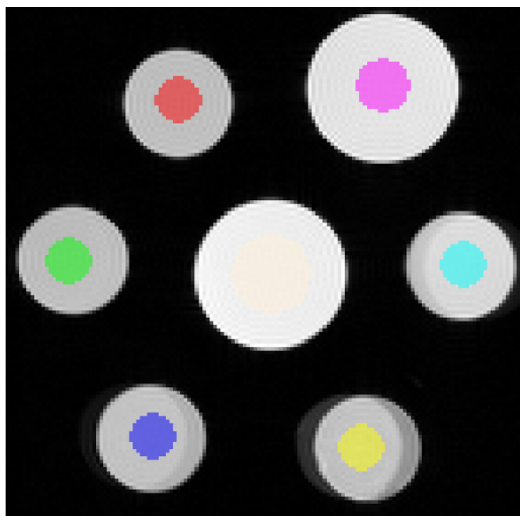


Figure 10: Example of phantom ROIs. Magnitude image of Dixon phantom with gadolinium and the different ROIs overlapped. The ROIs are composed of different circular regions (they can be seen in different colours) covering the inner part of every vial. ROIs were manually set in [ITK-SNAP](#) [71]

3.5 Statistical analysis

3.5.1 Statistical analysis: in-vivo

Due to the small size of the KO and WT groups' population, the nonparametric Mann-Whitney U test (or Wilcoxon rank-sum test) was used to statistically compare the distribution of both groups. The Mann-Whitney U test is a test of the null hypothesis that, for randomly selected values X and Y from two populations, the probability of X being greater than Y is equal to the probability of Y being greater than X . This test was performed with the MATLAB function [ranksum](#). If a p-value below 0.05 was obtained that would indicate that the rank-sum test rejects the null hypothesis of equal medians of both distributions at the default 5% significance level.

3.5.2 Correlation between Dixon and DWI in-vivo

To check if there exist any correlation between the 'pure' diffusion parameters (ADC and D) and the water fraction calculated from the mice brain, we performed Pearson and Spearman correlation tests. Pearson and Spearman correlation were computed region-wise between the mean of the 'pure' diffusion parameters values at 30 ms TE from both mono-exponential and IVIM models (ADC and D) and the mean water fraction for 6-point Dixon and 2 fatty acids double bonds. Two fatty acids double bonds were chosen for the correlation because more robust significant results were obtained from the *in-vivo* image analysis and more robust results are obtained from the

Dixon phantom validation results. Furthermore, it agrees with the assumption that fatty acids with 0, 1 and 2 fatty acids double bonds account for $\approx 97\% - 98\%$ of total fat in humans on ordinary Western diet [68]. The average was done over the 6 KOs and 4 WTs that underwent the complete MRI protocol (including DWI and Dixon) for each segmented region. Furthermore, correlations were calculated only averaging KO or only averaging WT animals. Correlations between the standard deviations of the different parameters were also computed to check that the significant correlations in the mean values are not due to phase differences.

3.5.3 Statistical analysis: ex-vivo

To characterize the different phantom compartments, one circular ROI was manually set in *ITK-SNAP* [71] for every vial, covering its inner part and excluding the borders because of higher partial volume (see example in the Figure 10).

T1 and T2 mean and standard deviation values of the aggregated voxels within each ROI were calculated. The $mean \pm SD$ T1 and T2 values characterized the different fat fraction emulsions.

The averages of the WF and FF of the voxels within every ROI were calculated to characterize the WF and FF of the different fat content emulsions in the phantoms.

4 Results

4.1 In-vivo imaging

4.1.1 DWI

Significant differences between KO and WT mice were found predominantly for the slow diffusion (ADC and D) parameters in different brain regions, from images acquired with both 22 *ms* and 30 *ms* TEs.

DWI at 22 *ms* TE

The probability that KO and WT groups have the same diffusivity parameters distributions in the different brain ROIs, obtained from the Wilcoxon Ranksum test performed between the 6 WTs and the 6 KOs, are shown in Table 9

Table 9: Wilcoxon ranksum test p-values between 6 KOs and 6 WTs diffusivity parameters at 22 *ms* TE. NS- no significance. Green color represents trend results with $0.15 > \text{p-value} > 0.05$ and red color represents significant results with $\text{p-value} < 0.05$

Region	ADC Model	IVIM Model			
	<i>ADC</i>	<i>D</i>	<i>D*</i>	<i>PF</i>	<i>FD*</i>
Olfactory	0.026	0.065	NS	NS	NS
Caudoputamen	NS	0.015	NS	NS	NS
Lateral Ventricle	NS	NS	0.093	NS	NS
Substantia Nigra	NS	NS	NS	NS	NS
Hippocampus	0.132	0.041	NS	NS	NS
Cingulate	NS	NS	0.093	NS	NS
Third Ventricle	NS	NS	NS	NS	NS
Cortex V1	NS	NS	NS	NS	NS
Cortex S1	NS	NS	NS	NS	NS
Cortex Auditory	NS	0.041	NS	NS	NS
Thalamus	0.132	0.015	NS	NS	NS
Hypothalamus	NS	NS	NS	NS	NS

In the Tables 9 and 10, color red is used to highlight the significant difference with $\text{p-value} < 0.05$, whereas color green is used to highlight the trend results, with $0.15 > \text{p-value} > 0.05$. *NS* means no significant result is obtained.

From the Table 9, we find significant difference in the *ADC* coefficient from the mono-exponential model between KO and WT in the olfactory

area. Here, no significant difference was found with the IVIM model, although there was trend for the slow diffusion parameter. Still, a significant difference in D , the slow diffusion parameter, was revealed in the caudoputamen, hippocampus, cortex auditory and thalamus.

No significant difference was found for D^* , the fast diffusion coefficient, although there was a trend for the lateral ventricle and the cingulate area between KO and WT.

Higher ADC and D coefficients were found in KO than in WT in the regions where significant differences were found.

DWI at 30 ms TE

DWI at 30 *ms* TE was performed in the same group of 6 KOs and 6 WT. The Wilcoxon Ranksum test was performed between WT and KO diffusivity parameters for statistical difference.

The probability that KO and WT groups have the same diffusivity parameters distributions in the different brain ROIs are shown in Table 10.

Table 10: Wilcoxon ranksum test p-values between 6 KOs and 6 WT. NS- no significance. Green color represents trend results with $0.15 > p\text{-value} > 0.05$ and red color represents significant results with $p\text{-value} < 0.05$

Region	ADC Model	IVIM Model			
	ADC	D	D^*	PF	FD^*
Olfactory	0.065	NS	NS	NS	NS
Caudoputamen	0.0086	0.0151	NS	NS	NS
Lateral Ventricle	NS	NS	NS	NS	NS
Substantia Nigra	NS	0.093	NS	NS	NS
Hippocampus	0.093	0.065	NS	NS	NS
Cingulate	NS	NS	NS	NS	NS
Third Ventricle	NS	NS	NS	NS	NS
Cortex V1	0.093	0.093	NS	NS	NS
Cortex S1	0.041	0.041	NS	NS	NS
Cortex Auditory	0.015	0.041	NS	NS	NS
Thalamus	0.0087	0.0087	NS	NS	0.132
Hypothalamus	NS	NS	NS	NS	NS

From Table 10, it is visible that both ADC and D provided similarly consistent results. The largest difference between KO and WT was visible

for both ADC and D in the caudoputamen, thalamus, cortex S1 and auditory. A trend is visible for ADC and D in the visual (V1) cortex and the hippocampus. We also find trend in ADC in olfactory, in D in substantia nigra and in FD^* in thalamus.

Higher ADC and D coefficients were found in KO than in WT in the regions where significant differences were found.

DWI at 22 ms TE vs. 30 ms TE

At 22 ms TE, a significant difference between KO and WT was found in 5 regions with $p < 0.05$ and trend was found in 5 regions with $p < 0.15$. At 30 ms TE significant difference between KO and WT was found in 8 regions with $p < 0.05$ and trend was found in 7 regions with $p < 0.15$. At 22 ms TE, ADC model provides significant differences in one region and trend in 2 regions whereas, IVIM model reveals majority of the findings, as significant difference in 4 regions and trend in 3 regions. At 30 ms TE ADC model finds significant difference in 4 regions and trend in 3 regions whereas IVIM model finds significant difference in 4 regions and trend in 4 regions. Overall, more significant differences were found at 30 ms TE than at 22 ms TE.

For the IVIM parameters, significant differences were found in 8 regions (4 at 22 ms TE and 4 at 30 ms TE) for the slow diffusion parameter, D , whereas no difference was found for pseudo perfusion parameters.

MR-DWI obtained with 22 ms and 30 ms TEs, showed similar results in D in the caudoputamen, cortex auditory and thalamus. At 30 ms TE, this significant difference is also found in ADC and the cortex area is extended to S1. However, at 30 ms TE we lose significant difference in D in the hippocampus and ADC in the olfactory area, where we find trend.

Still, using 30 ms TE more significant and robust results were obtained using both ADC (mono-exponential model) and IVIM (biexponential) models. This may indicate a presence of other factors influencing the signal at lower echo times. Those may be connected with increased ghosting, or increased presence of physiological pulsations. Hence, further correlation analysis to Dixon imaging considered only the DWI findings from 30 ms TE acquisition.

4.1.2 Dixon

Dixon was performed in 9 KOs and 7 WTs. The Wilcoxon Ranksum test was performed between the two groups for statistical difference in the WF.

To compare with the DWI subgroup, Wilcoxon Ranksum test was also performed between the 6 KOs and 4 WT's that underwent complete Dixon/DWI protocol.

Significant difference in WF was found in the pallidum under the assumption of 6 fatty acids double bonds, in the hippocampus under the assumption of 1, 2 and 6 fatty acids double bonds and in the periaqueductal gray under the assumption of 0, 1 and 2 fatty acids double bonds. The WF box plots for KO and WT groups of the significant difference results are shown in Figure 11.

In the groups that underwent also DWI at 30 *ms* TE, significant differences were found in the pallidum assuming presence of 6 fatty acids double bonds. However, no significant differences were found in the hippocampus and periaqueductal gray. This loss of significance for trend with respect to the complete set of animals with the Dixon sequence could be due to the small size subgroup's population.

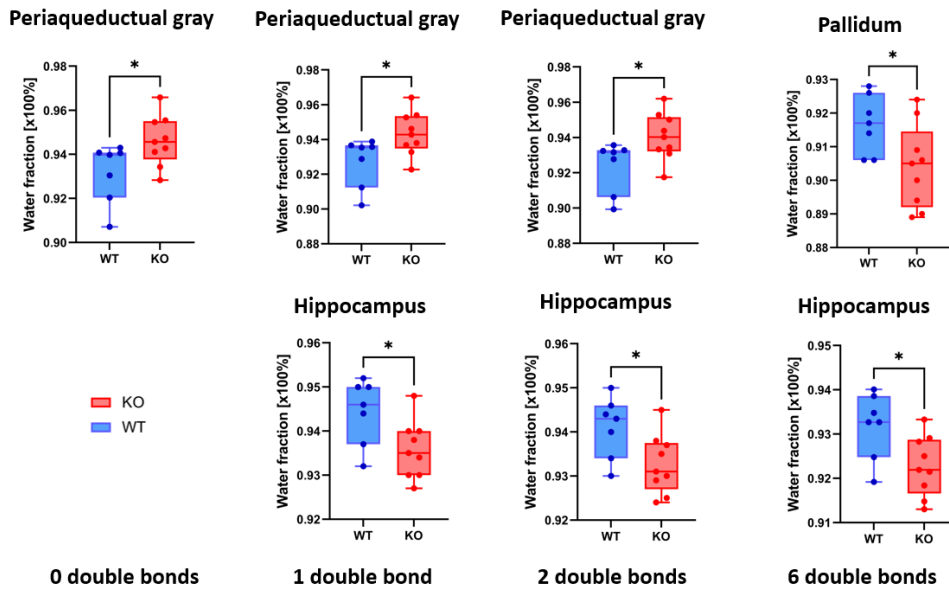


Figure 11: Whiskers-box plots for significantly different between 9 KO and 7 WT brain water fraction (WF) estimates *in-vivo*, found among 3 anatomical regions. 0, 1, 2 and 6 fatty acids double bonds (double bonds) are assumed in column 1, 2, 3 and 4, respectively.

4.2 Region-wise DWI-Dixon correlation

Correlation between the mean of slow diffusion parameters, ADC and D, at 30 *ms* TE, and the mean the WF under the assumption of two fatty acids double bonds was performed. Two fatty acids double bonds was chosen for correlation because a low number of fatty acids double bonds is expected within the brain [69] and more robust results were obtained in *in-vivo* and *ex-vivo* image analysis. The averaging was performed over the 6 KOs and 4 WTs and separately over the KOs and WTs, for every brain ROI separately.

Correlation was measured by means of linear Pearson’s and non-linear Spearman’s correlation. Only a significant correlation ($> 50\%$, $p < 0.05$ and non-zero slope) was obtained between mean WFs and mean D values in WT group using Spearman correlation ($r = 0.68$, $p - value = 0.035$).

4.3 Ex-vivo imaging

4.3.1 Water phantom with gadolinium contrast

T1 mapping using VTR

The T1 relaxation times obtained after VTR fitting (equation 22) for the different gadolinium concentrations are shown in Table 11. The *mean* \pm *SD* T1 relaxation times obtained before B_1^+ radio-frequency field inhomogeneity correction are shown in the first column.

The magnitude image of the mean of all RAREVTR images (from all TRs) is shown in the Figure 12A. The T1 map for the water phantom before applying B_1^+ correction is shown in Figure 12B.

Table 11: T1 relaxation times of the different gadolinium concentrations diluted in aCSF in the water phantom before (No B_1^+ correction) and after (B_1^+ correction) applying B_1^+ radio frequency field inhomogeneity correction.

	$T1$ [<i>ms</i>] No B_1^+ correction	$T1$ [<i>ms</i>] B_1^+ correction
aCSF +0.01 mM/mL Gd	19.9 ± 1.0	18.8 ± 1.2
aCSF +0.001 mM/mL Gd	189.9 ± 1.2	183.9 ± 3.6
aCSF +0.0001 mM/mL Gd	1064.2 ± 11.3	909.7 ± 41.4
aCSF	2786.8 ± 35.5	1866.0 ± 197.4

B_1^+ radio-frequency transmit field inhomogeneity correction

After applying B_1^+ radio-frequency field inhomogeneity correction, the $mean \pm SD$ T1 relaxation times obtained for the different gadolinium concentrations are shown in the second column in Table 11.

The B_1^+ correction map obtained after using the double angle method is shown Figure 12B. The T1 map for the water phantom after applying B_1^+ correction is shown in Figure 12D.

From Table 11, it can be seen that T1 relaxation time decreases with an increasing gadolinium concentration, as expected. Also, the bias of T1 estimation for B_1^+ -uncorrected images increases for compartments of longer T1 times. Therefore, we can compare the aCSF T1 relaxation time with different values reported on literature. Stark and Bradley in Magnetic Resonance imaging (p 44) [82] reported CSF $T1 = 2350 \text{ ms}$ relaxation time at 1.5 T . Whereas Lu et al. [83] found CSF $T1 = 3836 \pm 470 \text{ ms}$ relaxation time at 1.5 T and $T1 = 3817 \pm 424 \text{ ms}$ at 3 T .

Overall, T1 relaxation times have decreased after applying B_1^+ correction.

Respective T1 fittings of aggregated voxels intensity distribution within each vial of the water phantom before and after applying B_1^+ correction are shown in Figure 13. The fittings include, fitting curve (equation 22) with mean M_0 , T1 and additive error of aggregated voxels intensity distribution and its 95% confidence interval (CI). Errorbars with the $mean \pm 1 \cdot SD$ signal intensity of aggregated voxels intensity distribution are also represented for both B_1^+ and no B_1^+ corrected values. Figure 13A shows the fittings for aCSF and corresponds to vial 2 in Figure 12. Figure 13B shows the fittings for aCSF +0.0001 mM/mL Gd and corresponds to vial 3 in Figure 12. Figure 13C shows the fittings for aCSF +0.001 mM/mL Gd and corresponds to vial 1 in Figure 12. And Figure 13D shows the fittings for aCSF +0.01 mM/mL Gd and corresponds to vial 4 in Figure 12.

Based on the results obtained we chose a 0.001 mM/mL gadolinium concentration as our working concentration for the water-fat Dixon phantom, as allowing to obtain a good signal amplitude for TEs $> 2 \text{ ms}$ and TR of 750 ms (i.e. > 3 times T1 estimated) applied in MGE Dixon sequence (Tables 4, 6 and 8).

T2 mapping

The magnitude image of the mean of all echo images in the MSME acquisition is shown in Figure 14A.

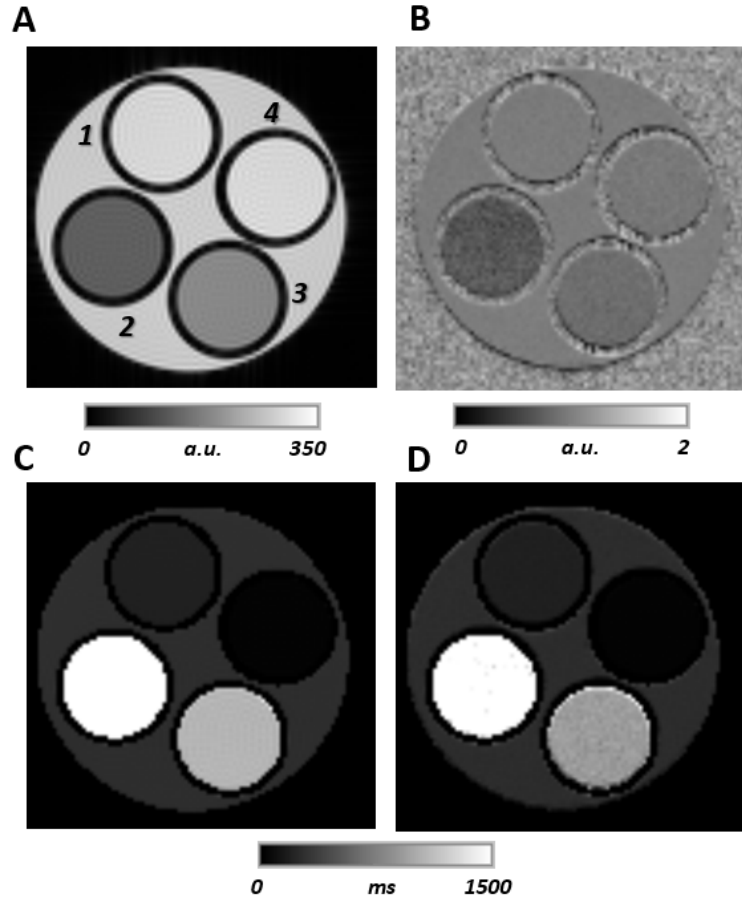


Figure 12: Water phantom T1 mapping. A: Magnitude RAREVTR image (mean of all images in the acquisition); B: B_1^+ map used for T1 map correction; C: T1 map before the B_1^+ correction; D: T1 map after the B_1^+ correction. Different vials are: 1-aCSF +0.001 mM/mL Gd; 2-aCSF; 3-aCSF +0.0001 mM/mL Gd; 4-aCSF +0.01 mM/mL Gd.

The T2 relaxation times obtained after fitting voxel-wise the signal intensity to equation 26 are shown in Table 12.

Table 12: T2 relaxation times of the different gadolinium concentrations diluted in aCSF in the water phantom.

	$T2$ [ms]
aCSF +0.01 mM/mL Gd	13.9 ± 0.6
aCSF +0.001 mM/mL Gd	91.0 ± 0.6
aCSF +0.0001 mM/mL Gd	215.4 ± 4.4
aCSF	231.6 ± 8.6

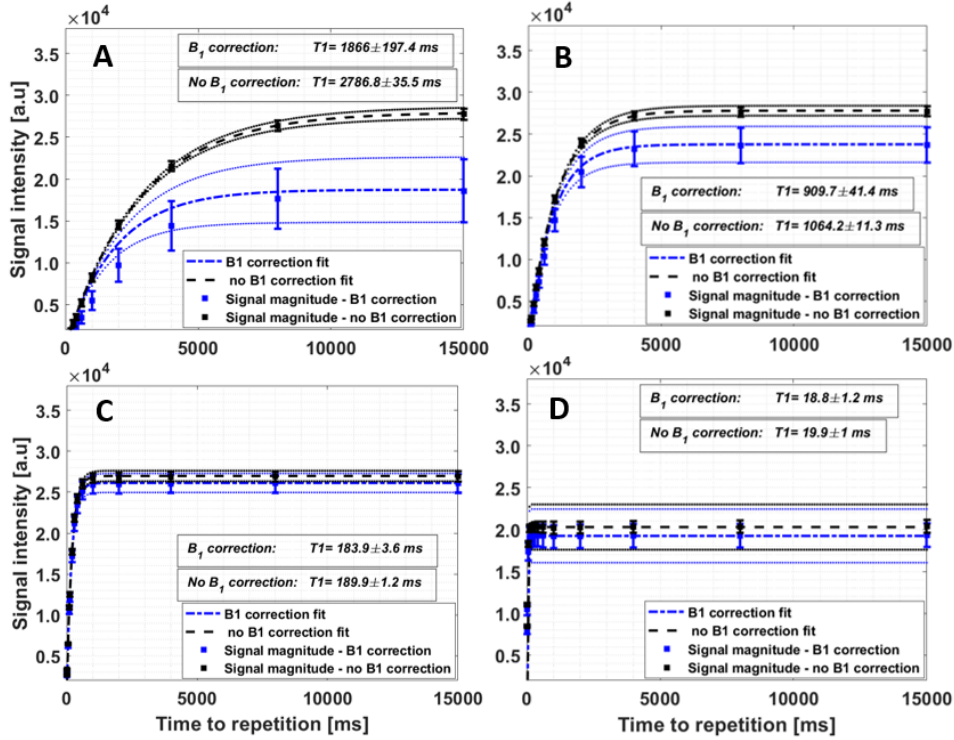


Figure 13: T1 fittings before and after applying B_1^+ , along with means and SD of aggregated voxel intensities at respective TR, in each water phantom vial. The fittings include, fitting curve (eq. 26) with mean M_0 , T_1 and additive error of aggregated voxels intensity distribution and its 95% CI. Errorbars with the mean and 1SD of aggregated voxels intensities are also represented for both B_1^+ and no B_1^+ corrected values. A: aCSF (vial 2 in Figure 12); B: aCSF +0.0001 mM/mL Gd (vial 3 in Figure 12); C: aCSF +0.001 mM/mL Gd (vial 1 in Figure 12); D: aCSF +0.01 mM/mL Gd (vial 4 in Figure 12).

From Table 12, it can be seen that T2 relaxation time decreases with increasing gadolinium concentration, as expected. We can compare the aCSF T2 relaxation time with different values reported on literature. Stark and Bradley in Magnetic Resonance imaging [82] (page 44) reported CSF $T_2 = 180 \text{ ms}$ relaxation time at 1.5 T. Although O'Reilly et al. [84] reported higher T2 relaxation times at 50 mT with $mean \pm SD T_2 = 1584 \pm 124 \text{ ms}$. *In-vivo* measurements at 9.4 T [85] reported water T2 relaxation times in different rat brain regions between $T_2 = 35.8 \pm 1.2 \text{ ms}$ in corpus callosum and $T_2 = 48.1 \pm 1.9 \text{ ms}$ in olfactory bulb.

The T2 map for the water phantom is shown in Figure 14B.

The T2 fittings of aggregated voxel intensities within each vial of the water phantom are shown in the Figure 15. The fittings include, fitting curve

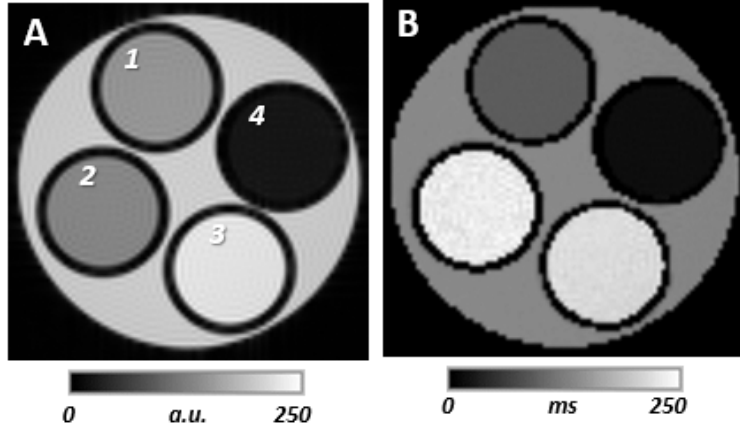


Figure 14: A: Magnitude image of the mean of all echo images in the MSME acquisition; B: T2 map. The different vials are: 1-aCSF+0.001 mM/mL Gd; 2-aCSF; 3-aCSF+0.0001 mM/mL Gd; 4-aCSF+0.01 mM/mL Gd.

(equation 26) with mean M_0 , T_2 and additive error of aggregated voxels intensities and its 95% CI. Errorbars with the $mean \pm 1 \cdot SD$ signal intensity of aggregated voxels intensities are also plotted. Figure 15A shows the fittings for aCSF and corresponds to vial 2 in Figure 14. Figure 15B shows the fittings for aCSF +0.0001 mM/mL Gd and corresponds to vial 3 in Figure 14. Figure 15C shows the fittings for aCSF +0.001 mM/mL Gd and corresponds to vial 1 in Figure 14. And Figure 15D shows the fittings for aCSF +0.01 mM/mL Gd and corresponds to vial 4 in Figure 14.

Dixon IDEAL algorithm

To verify, whether it is possible to quantify the fat content based on the signal alteration due to paramagnetic relaxation times shortening, Dixon quantification was performed in the water phantom (see section 3.2.2). From calculated water-only and fat-only Dixon images by means of the Dixon IDEAL algorithm using the complete 6 echoes set of the MGE sequence, a water and fat fraction maps were estimated. Next, the estimation was performed using only the first four echoes and the last four echoes. All calculations were done under assumptions of 0, 1, 2 and 6 fatty acids double bonds. The obtained FF (in %) were further obtained (see Table 13).

The sequence using the first four echoes depicts slightly higher fat fractions than the other two sequences, especially for the highest gadolinium concentration and up to 3.06% under the 6 fatty acids double bonds assumption. All three approaches using different TE sets depict increasing fat fractions for increasing number of the fatty acids double bonds assumed.

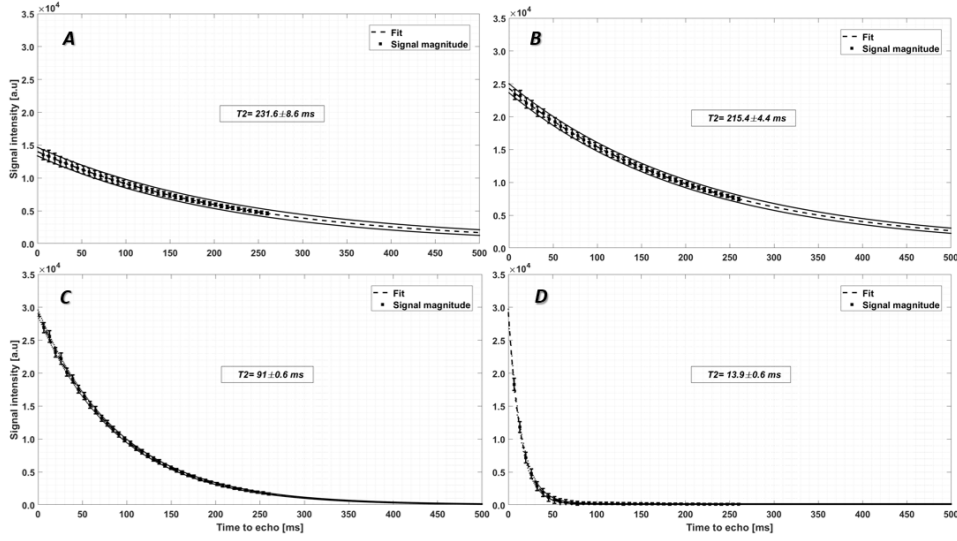


Figure 15: T2 fittings of aggregated voxel intensities within each vial. The charts include, fitting curves (eq. 26) along with mean M_0 , T_2 and 95% CI for the fitting. Errorbars with the mean and 1SD of aggregated voxel intensities at each TE are also plotted. A: aCSF (vial 2 in Figure 14); B: aCSF+0.0001 mM/mL Gd (vial 3 in Figure 14); C: aCSF+0.001 mM/mL Gd (vial 1 in Figure 14); D: aCSF+0.01 mM/mL Gd (vial 4 in Figure 14).

Table 13: The results for the fat fraction (FF) estimation in the water phantom with gadolinium tracer of various concentration. FF was calculated (in %) under the assumption of 0, 1, 2 and 6 fatty acids double bonds (Double bonds).

	Double bonds	0.01 mM/mL Gd	0.001 mM/mL Gd	0.0001 mM/mL Gd	aCSF
		FF(%)	FF(%)	FF(%)	FF(%)
1st – 4th echoes	0	1.56	0.22	1.11	0.47
	1	1.91	0.40	1.33	0.76
	2	2.34	0.69	1.53	1.12
	6	3.06	1.31	1.43	1.81
3rd – 6th echoes	0	0.71	0.67	0.81	0.72
	1	0.65	0.66	0.86	0.65
	2	0.59	0.63	0.88	0.55
	6	0.96	0.61	1.01	0.69
All 6 echoes	0	0.57	0.32	0.44	0.40
	1	0.60	0.33	0.51	0.42
	2	0.63	0.35	0.57	0.44
	6	0.72	0.41	0.75	0.52

This should be expected as the correct assumption in the water phantom is

0 fatty acids double bonds. It is also worth to highlight, that the phantom vial filled with aCSF +0.001 mM/mL gadolinium concentration (here, chosen working concentration based on T1 and T2 estimates) provided overall the lowest bias of estimates. The worst estimates assuming the highest FF were obtained using the highest gadolinium concentration (0.01 mM/mL), which is characterized by the strongest T1 and T2 shortening (see section 2.1.4).

A magnitude image of the sum of all 6 echoes of the MGE acquisition for the water phantom is shown in Figure 16A.

The water-only and fat-only images of the water phantom under the assumption of 2 fatty acids double bonds are shown in Figure 16B, in Fat and Water columns, respectively. The top row corresponds to the first four echoes images, the middle row corresponds to the last four echoes images and the bottom row corresponds to all 6 echoes images.

4.3.2 Dixon phantom with gadolinium contrast

T1 mapping using VTR

The T1 relaxation times obtained after VTR fitting (equation 22) for the aCSF and the different fat content solutions are shown in Table 14. The $mean \pm SD$ T1 relaxation times obtained before B_1^+ radio-frequency field inhomogeneity correction are shown in the first column. For reference, the mean RAREVTR image (from all TRs) is shown in the Figure 17A.

The T1 relaxation time obtained for the 100% fat content solution (which doesn't contain Gd) is $T1 = 545.7 \pm 8.3$. This value is similar to those found in literature. For instance, Sindi et al. [86] reported a $T1 = 405.4 \pm 15.1 ms$ relaxation time for peanut oil at 3 T and Jordan et al. [87] reported in two different measurements $T1 = 280 ms$ and $T1 = 281 ms$ at 3 T and $T1 = 433 ms$ and $T1 = 435 ms$ at 7 T .

Decreasing fat content within the phantom vials made from 3% agarose along with 0.001 mM/mL gadolinium were found to be associated with decreasing T1 estimates. As we previously found the working gadolinium concentration to shorten the T1 time $< 200 ms$ in the aCSF, the phenomena was confirmed here. Moreover, it seems that the agarose solution provide additional properties of slightly altering the T1 found (see Table 14 aCSF 0.001 mM/mL Gd vs. 0% FF). Also, the T1 estimates for the low fat content (i.e. 2% FF) seem very close to those obtained from aCSF +0.001 mM/mL Gd. This may explain the previous findings, that certain concentrations of

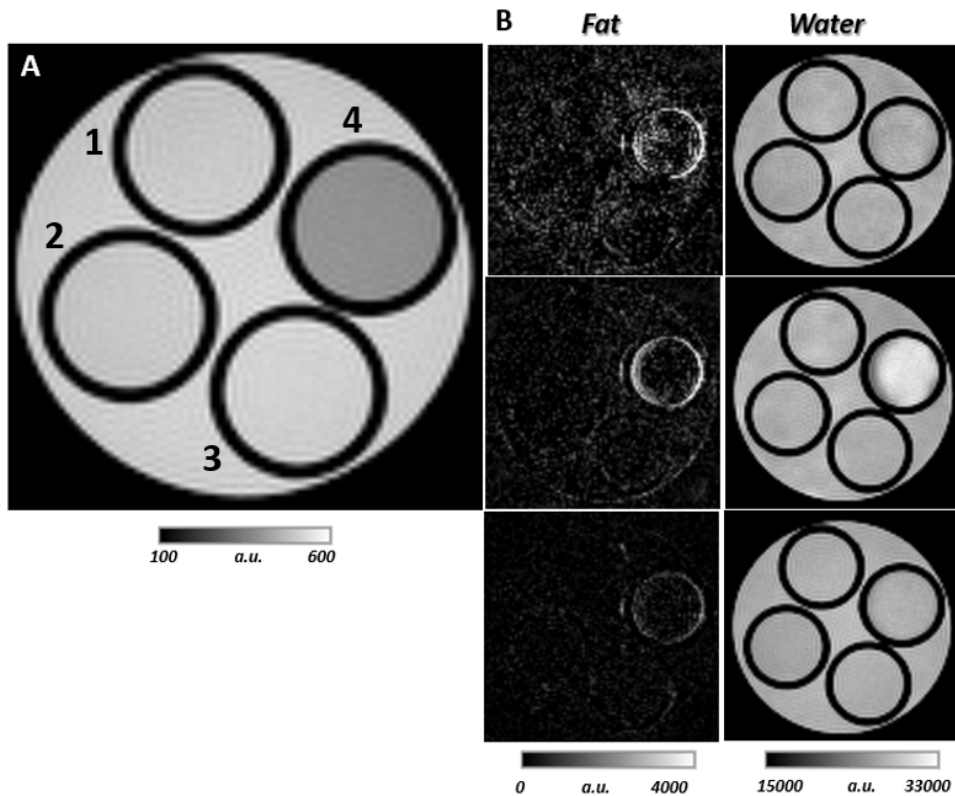


Figure 16: Images for the water phantom Dixon results. A: Magnitude image of the sum of all 6 echoes of the MGE acquisition. B: Only-fat (Fat column) and only-water (Water column) images of the Dixon phantom under the assumption of 2 fatty acids double bonds. Top row: first four echoes image; middle row: last four echoes image; bottom row: all 6 echoes image. The different vials are: 1-aCSF+0.001 mM/mL Gd; 2-aCSF; 3-aCSF+0.0001 mM/mL Gd; 4-aCSF+0.01 mM/mL Gd.

Gd may mimic the contribution from low concentration fat to MR signal (see Table 13). The T1 estimates obtained for different fat content solutions within the phantom are difficult to compare since they have different fat content and Gd concentrations, and both conditions, increasing fat content and increasing Gd concentration, have a decreasing effect in the T1 relaxation times.

The T1 map for the Dixon phantom with gadolinium before applying B_1^+ correction is shown in Figure 17C.

B_1^+ field inhomogeneity correction

After applying B_1^+ radio-frequency field inhomogeneity correction, the $mean \pm SD$ T1 relaxation times obtained for the aCSF and the different fat

Table 14: T1 relaxation times of the aCSF and the different fat fractions before (No B_1^+ correction) and after (B_1^+ correction) applying B_1^+ radio frequency field inhomogeneity correction.

	$T1$ [ms] No B_1^+ correction	$T1$ [ms] B_1^+ correction
aCSF	2914.7 ± 30.6	2614.5 ± 46.3
aCSF +0.001 mM/mL Gd	171.2 ± 3.8	210.4 ± 4.7
0% FF	201.9 ± 4.5	246.9 ± 5.5
2% FF	193.3 ± 4.8	236.1 ± 6.0
10% FF	226.9 ± 5.3	278.3 ± 6.6
25% FF	267.0 ± 6.5	327.9 ± 8.2
100% FF	465.0 ± 7.0	545.7 ± 8.3

content solutions are shown in the second column in Table 14.

The B_1^+ correction map obtained after using the double angle method is shown Figure 17B.

The T1 map for the Dixon phantom with gadolinium after applying B_1^+ correction is shown in Figure 17D.

To verify the T1 values obtained after B_1^+ radio-frequency field inhomogeneity correction, two IR RARE sequences were employed to verify the signal cancellation in the main vials consisting of 100% FF (pure oil without gadolinium) and a FF value between 10% and 25% (with gadolinium), using inversion pulses of 500 (see Figure 17F) and 300 ms (see Figure 17E), respectively.

The T1 fittings of the aggregated voxels intensity distribution within each vial of Dixon phantom with gadolinium, before and after applying B_1^+ correction, are shown in Figure 18 and Figure 19. The fittings include: fitting curve (equation 22) with mean M_0 , $T1$ and additive error of aggregated voxels intensities and its 95% CI; errorbars with the $mean \pm 1 \cdot SD$ signal intensity of aggregated voxels are also represented for both B_1^+ and no B_1^+ corrected values. Figure 18A shows the fittings for aCSF and corresponds to vial 5 in Figure 17. Figure 18B shows the fittings for aCSF +0.001 mM/mL Gd and corresponds to vial 6 in Figure 17. Figure 18C shows the fittings for 0% FF and corresponds to vial 1 in Figure 17.

Figure 19A shows the fittings for 2% fat content solution and corresponds to vial 2 in Figure 17. Figure 19B shows the fittings for 10% fat content solution and corresponds to vial 3 in Figure 17. Figure 19C shows the fittings

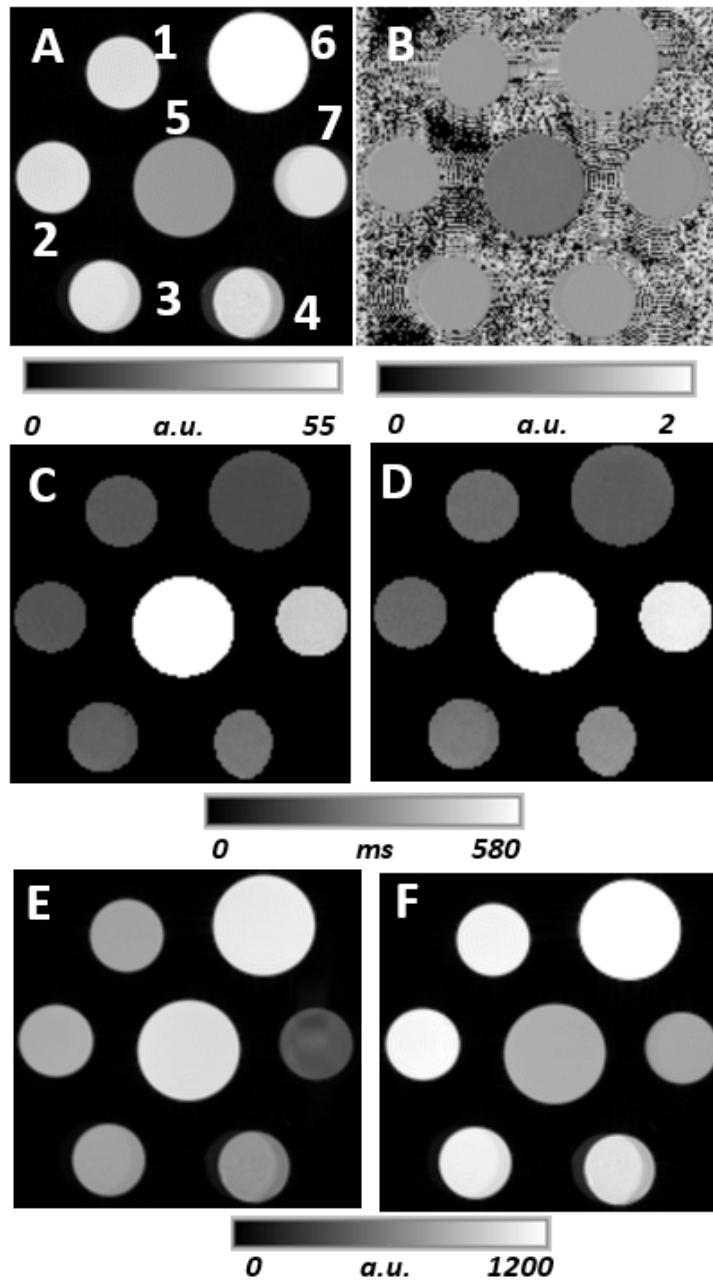


Figure 17: Dixon phantom with gadolinium T1 results. A: Magnitude image of the mean of all images in the RAREVTR acquisition. B: B_1^+ map used for T1 map field inhomogeneities correction. C: T1 map before B_1^+ correction. D: T1 map after B_1^+ correction. E and F: IR RARE magnitude images acquired at inversion recovery times 300 and 500 ms, respectively, to measure the signal cancellation in the main vials. The different vials are: 1-0% FF; 2-2% FF; 3-10% FF; 4-25% FF; 5-aCSF; 6-aCSF+0.001 mM/mL Gd; 7- 100% FF.

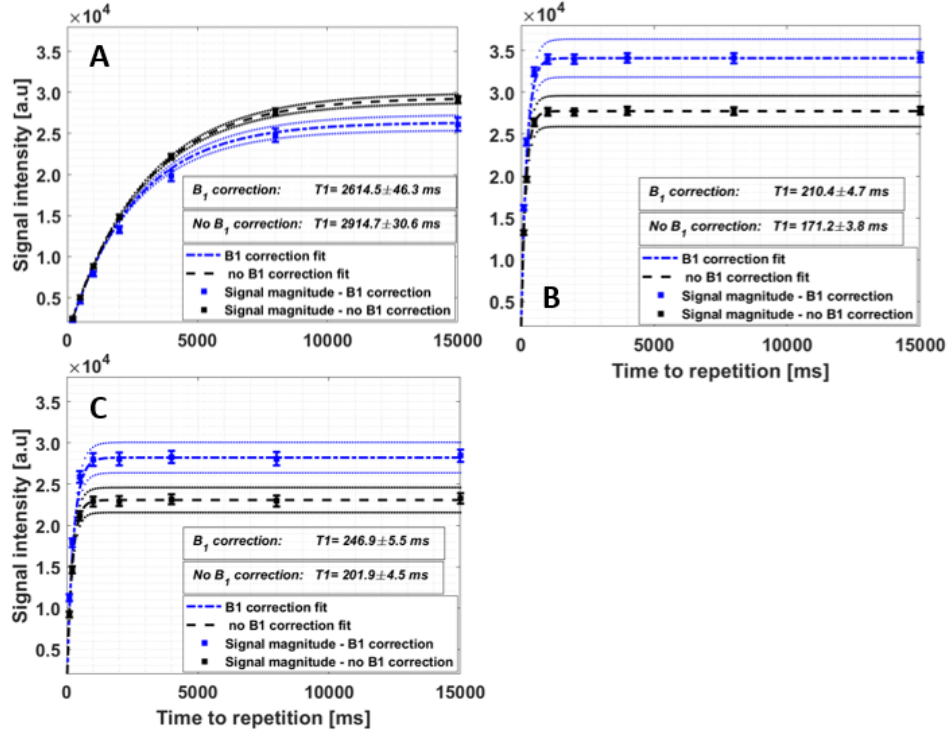


Figure 18: B_1^+ and no B_1^+ corrected T1 fittings of aggregated voxels intensity distribution within each vial. Fittings include, fitting curve (eq. 26) with mean M_0 , T1 and additive error of aggregated voxels intensities and its 95% CI. Errorbars with the mean and 1SD of aggregated voxels intensities are also represented for both B_1^+ and no B_1^+ corrected values. A: aCSF (vial 5 in Figure 17); B: aCSF+0.001 mM/mL Gd (vial 6 in Figure 17); C: 0% fat content (vial 1 in Figure 17);

for 25% fat content solution and corresponds to vial 4 in Figure 17. Figure 19D shows the fittings for 100% fat content solution and corresponds to vial 7 in Figure 17.

Overall, T1 relaxation time increases with increasing fat content. Furthermore, the presence of agarose 3% increases the T1 relaxation time.

T2 mapping

The magnitude image of the mean of all echo images in the MSME acquisition for the Dixon phantom is shown in Figure 20A.

The T2 relaxation times obtained after fitting voxel-wise the signal intensity to equation 26 are shown in Table 15. And the T2 map for the Dixon phantom with gadolinium is shown in Figure 20B.

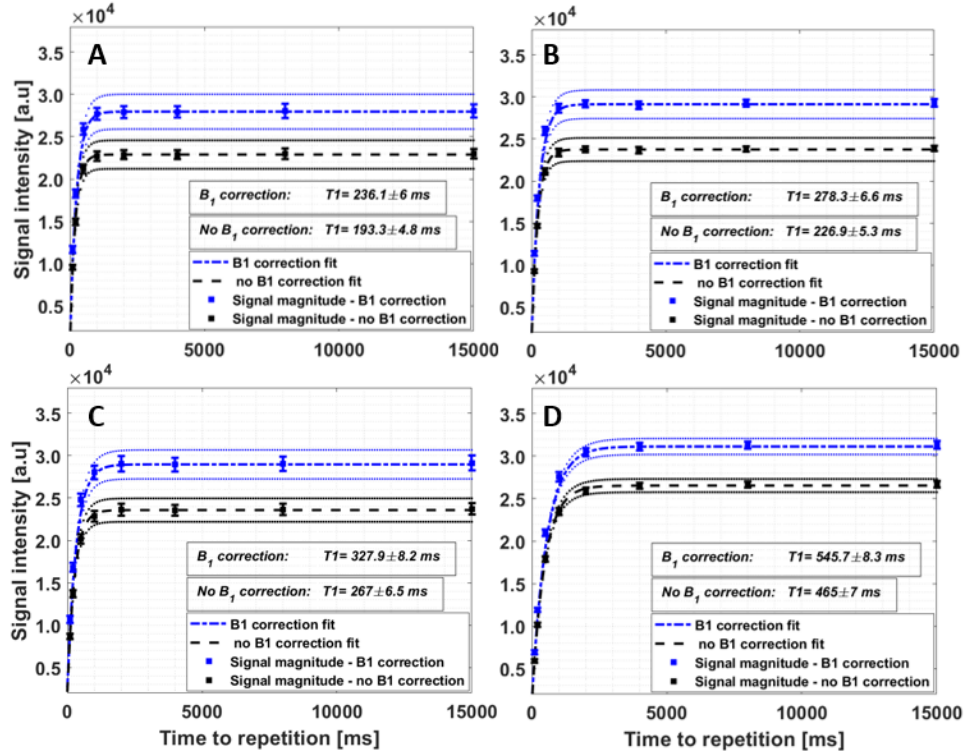


Figure 19: B_1^+ and no B_1^+ corrected T1 fittings of aggregated voxels intensity distribution within each vial. Fittings include, fitting curve (eq. 26) with mean M_0 , T_1 and additive error of aggregated voxels intensities and its 95% CI. Errorbars with the mean and 1SD of aggregated voxels intensities are also represented for both B_1^+ and no B_1^+ corrected values. A: 2% fat content (vial 2 in Figure 17); B: 10% fat content (vial 3 in Figure 17); C: 25% fat content (vial 4 in Figure 17); D: 100% fat content (vial 7 in Figure 17).

Table 15: T2 relaxation times of the different solutions in the Dixon phantom with gadolinium.

	T_2 [ms]
aCSF	238.7 ± 4.8
aCSF +0.001 mM/mL Gd	93.2 ± 0.3
0% FF	31.9 ± 0.9
2% FF	28.7 ± 0.2
10% FF	28.4 ± 0.1
25% FF	28.6 ± 0.2
100% FF	49.7 ± 0.1

The T2 relaxation time estimate obtained for the 100% fat content is

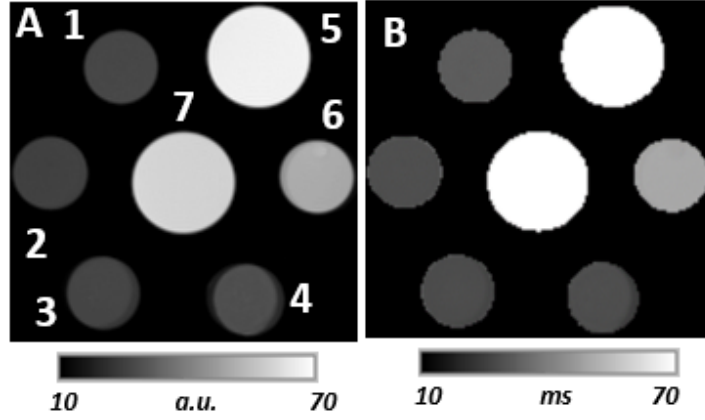


Figure 20: A: Magnitude image of the mean of all echo images in the MSME acquisition; B: T2 map. The different vials are: 1-0% fat content; 2-2% fat content; 3-10% fat content; 4-25% fat content; 5-aCSF; 6-aCSF+0.001 mM/mL Gd; 7- 100% fat content.

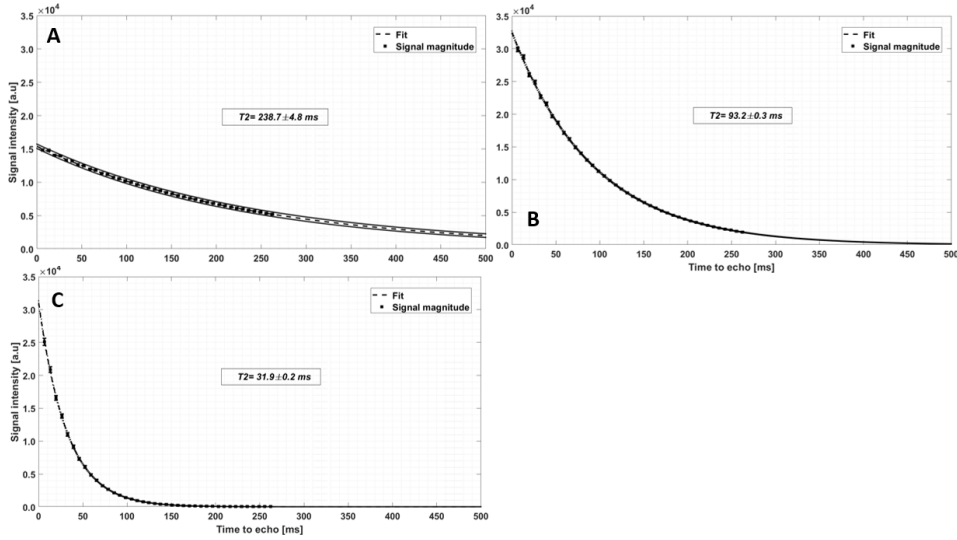


Figure 21: T2 fittings of aggregated voxels intensity distribution within each vial. Fittings include, fitting curve (eq. 26) with mean M_0 , T_2 and additive error of aggregated voxels intensities and its 95% CI. Errorbars with the mean and $1SD$ of aggregated voxels intensities are also plotted. A: aCSF (vial 5 in Figure 17); B: aCSF+0.001 mM/mL Gd (vial 6 in Figure 17); C: 0% fat content (vial 1 in Figure 17);

similar to those found in literature. Jordan et al. [87] reported peanut oil $T_2 = 53.9 ms$ and $T_2 = 58.8 ms$ at 3.0 T and $T_2 = 43.4 ms$ and $T_2 = 42.7 ms$ at 7.0 T .

The T2 fittings of aggregated voxels intensity distribution within each vial in the Dixon phantom with gadolinium are shown in Figure 21 and Fig-

ure 22. The fittings include, fitting curve (equation 26) with mean M_0 , T_2 and additive error of aggregated voxels intensities and its 95% CI. Errorbars with the $mean \pm 1 \cdot SD$ signal intensity of aggregated voxels are also plotted.

Figure 21A shows the fittings for aCSF and corresponds to vial 5 in Figure 20. Figure 21B shows the fittings for aCSF +0.001 mM/mL Gd and corresponds to vial 6 in Figure 20. Figure 21C shows the fittings for 0% fat content and corresponds to vial 1 in Figure 20.

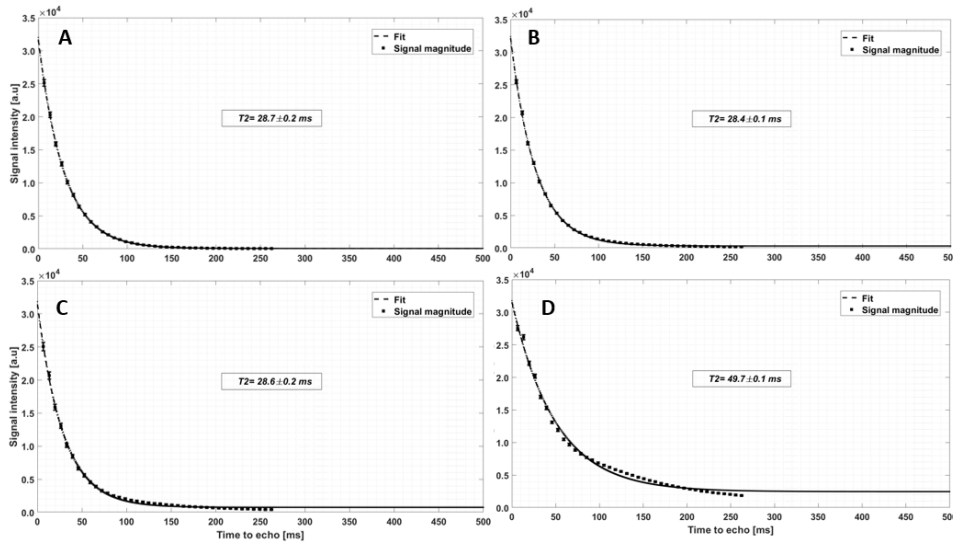


Figure 22: T2 fittings of aggregated voxels intensity distribution within each vial. Fittings include, fitting curve (eq. 26) with mean M_0 , T_2 and additive error of aggregated voxels intensities and its 95% CI. Errorbars with the mean and $1SD$ of aggregated voxels intensities are also plotted. A: 2% fat content (vial 2 in Figure 17); B: 10% fat content (vial 3 in Figure 17); C: 25% fat content (vial 4 in Figure 17); D: 100% fat content (vial 7 in Figure 17).

Figure 22A shows the fittings for 2% fat content solution and corresponds to vial 2 in Figure 20. Figure 22B shows the fittings for 10% fat content solution and corresponds to vial 3 in Figure 20. Figure 22C shows the fittings for 25% fat content solution and corresponds to vial 4 in Figure 20. Figure 22D shows the fittings for 100% fat content solutions and corresponds to vial 7 in Figure 20.

Dixon IDEAL algorithm

From the 6–point Dixon sequence, we calculated the water and fat fractions using the complete 6 echoes set of the MGE sequence; using the first four echoes and using the last for echoes under the assumptions of 0, 1, 2

and 6 fatty acids double bonds. The images were also corrected for B_1^+ radio-frequency field inhomogeneity and gaussian smoothed. However, no significant difference in the WF and FF was obtained between the original and the post-processed images. Therefore, in this section I will only present the results for the original images, using the first four echoes, the last four echoes and all the six echoes.

The obtained FF (in %) for the different echoes combinations and under the assumption of 0, 1, 2 and 6 fatty acids double bonds are shown in Table 16.

Table 16: Dixon phantom with gadolinium Dixon results. Fat fractions (FF) (in %) under the assumption of 0, 1, 2 and 6 fatty acids double bonds (D.B) for the different echoes combinations.

	D.B	aCSF FF (%)	0.001 mM/mL Gd FF(%)	0% FF(%)	2% FF(%)	10% FF(%)	25% FF(%)	100% FF(%)
1^{st} - 4^{th} echoes	0	2.31	5.02	0.47	0.84	4.89	19.99	33.51
	1	2.42	5.42	0.61	1.11	4.52	19.79	59.22
	2	2.59	4.39	0.98	1.45	3.99	16.90	68.56
	6	3.40	2.51	1.19	2.68	3.14	5.88	35.99
3^{rd} - 6^{th} echoes	0	0.81	1.03	1.79	0.96	0.78	5.39	98.59
	1	0.88	1.47	2.18	0.98	0.99	10.12	95.78
	2	0.98	2.35	2.63	0.98	1.32	14.99	70.58
	6	1.39	2.91	3.41	1.11	2.48	17.49	4.15
All 6 echoes	0	0.59	0.83	3.01	0.47	0.37	4.51	0.00
	1	0.66	0.94	3.42	0.45	0.14	2.19	0.00
	2	0.72	1.02	3.53	0.47	0.07	0.57	0.01
	6	0.89	1.09	2.91	0.69	0.10	0.03	0.51

Overall, the sequence including all 6 echoes fails to depict the correct fat fraction. It especially overestimates the FF for the 0% fat content compartment, which is especially visible in case of presence of 0.001 mM/mL Gd concentration in aCSF. The approaches including only first four and last four echoes provided correct estimates of the FF for higher fat content emulsions (> 10%). In particular, the first four echo sequence performs better than the last four echo sequence for the 10% and 25% fat content emulsions, whereas the last four echo sequence performs better than the first four echo sequence for the 100% fat content compartment. It can also be seen that the best results are obtained for 1 and 2 fatty acids double bonds.

In case aCSF +0.001 mM/mL Gd and 0% fat content compartments, all approaches wrongly overestimated the fat content. As mentioned before, it seems that certain concentration of gadolinium (and those mostly optimal for *in-vivo* application in preclinical setups, as here) can alter the separation of fat and water signals. This could be due to the presence of Gd, shortening the relaxation so that the fat component may appear to be mimicked. Therefore, there is a need to check the possible effect of Gd when depicting fat and water content by using a phantom without gadolinium.

A magnitude image of the sum of all 6 echoes of the MGE acquisition for the Dixon phantom with gadolinium is shown in the Figure 23A.

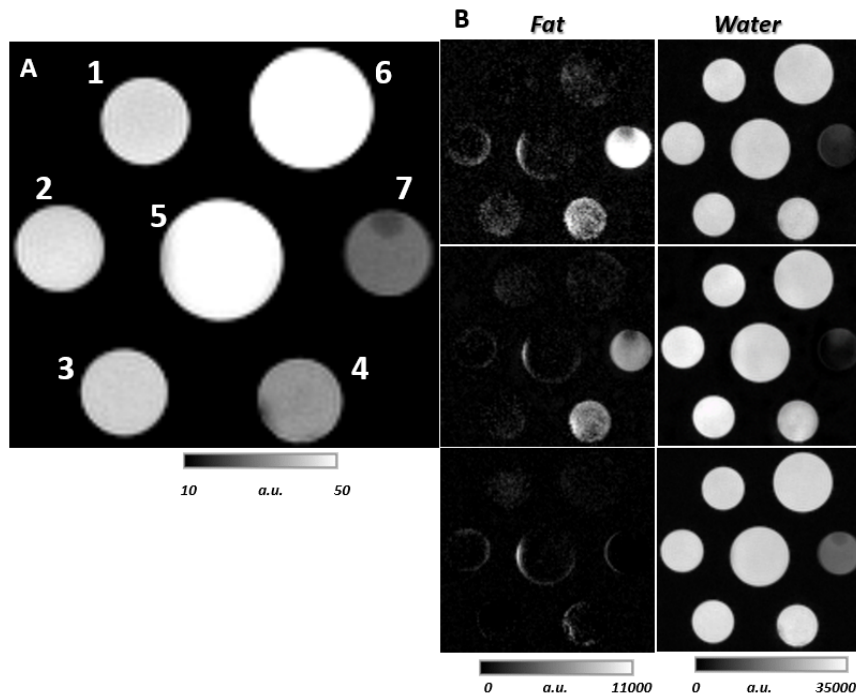


Figure 23: Dixon phantom with gadolinium Dixon results. A: Magnitude image of the sum of all 6 echoes of the MGE acquisition. B: Only-fat (Fat column) and only-water (Water column) images of the Dixon phantom under the assumption of 2 fatty acids double bonds. Top row: first four echoes image; middle row: last four echoes image; bottom row: all 6 echoes image. The different vials are: 1-0% fat content; 2-2% fat content; 3-10% fat content; 4-25% fat content; 5-aCSF; 6-aCSF+0.001 mM/mL Gd; 7-100% fat content.

The water-only and fat-only images of the Dixon phantom with gadolinium under the assumption of 2 fatty acids double bonds are shown in Figure 23B, in Fat and Water columns, respectively. The top row corresponds to the first four echoes images, the middle row corresponds to the last four echoes

images and the bottom row corresponds to all 6 echoes images.

4.3.3 Dixon phantom without gadolinium contrast

T1 mapping using VTR

The magnitude image of the mean of all images (of all TRs) in the RAREVTR acquisition for the Dixon phantom without gadolinium is shown in Figure 24A.

The T1 relaxation times obtained after VTR fitting (equation 22) for the different fat content are shown in Table 17. The $mean \pm SD$ T1 relaxation times obtained before B_1^+ radio-frequency field inhomogeneity correction are shown in the first column.

Table 17: T1 relaxation times of the different fat content solutions before (No B_1^+ correction) and after (B_1^+ correction) applying B_1^+ radio frequency field inhomogeneity correction.

	$T1$ [ms] No B_1^+ correction	$T1$ [ms] B_1^+ correction
0% FF	2755.7 ± 108.9	1747.2 ± 114.6
2% FF	2645.0 ± 100.8	1769.6 ± 108.9
10% FF	2259.1 ± 102.5	1644.4 ± 98.2
25% FF	1597.0 ± 105.8	1306.1 ± 95.8
50% FF	1945.9 ± 567.5	1430.0 ± 327.7
50% FF	2589.1 ± 116.0	1707.5 ± 151.0
100% FF	557.8 ± 63.4	524.1 ± 59.9

Overall, the T1 estimates from the Dixon phantom without gadolinium are markedly larger from those in the phantom containing gadolinium (see Table 14 vs. Table 17). From the Table 17, it can be seen that T1 relaxation time decreases with increasing fat content, as expected, since fat protons relax more rapidly than water protons. However, the T1 relaxation times of the two different 50% fat content emulsions don't follow this decreasing trend. This is because at this high fat content, the water and fat solutions didn't emulsify properly, and instead it presents differentiated fat and water layers that are not properly mixed (see Figure 9A). Therefore, probably a rather unknown proportion of water and fat was used in these vials.

The T1 map for the Dixon phantom without gadolinium before applying B_1^+ correction is shown in Figure 24C.

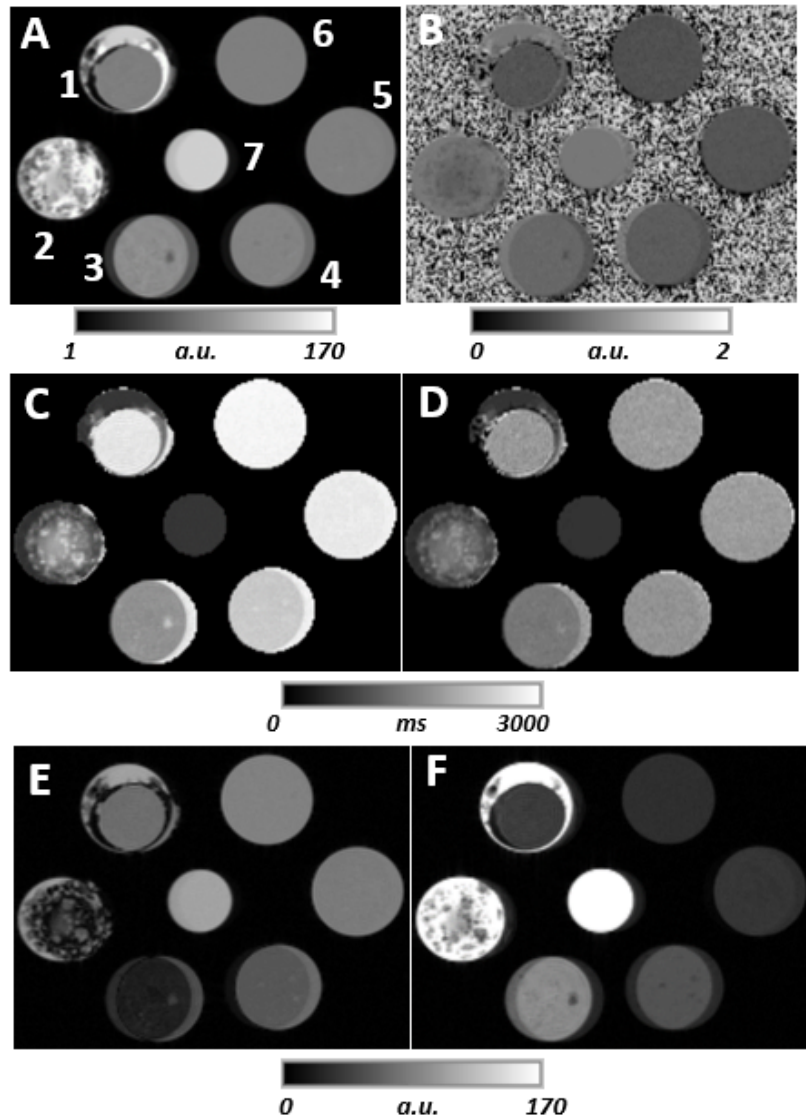


Figure 24: Dixon phantom without gadolinium T1 results. A: Magnitude image of the mean of all images in the RAREVTR acquisition. B: B_1^+ map used for T1 map field inhomogeneities correction. C: T1 map before B_1^+ correction. D: T1 map after B_1^+ correction. E and F: IR RARE magnitude images acquired at inversion recovery times 500 and 1500 *ms*, respectively, to measure the signal cancellation in the main vials. The different vials are: 1- 50% FF; 2- 50% FF; 3- 25% FF; 4-10% FF; 5-2% FF; 6-0% FF; 7-100%.

B_1^+ field inhomogeneity correction

The B_1^+ correction map obtained using the double angle method (see section 3.4.2) is shown Figure 24B. The T1 map for the Dixon phantom

without gadolinium after applying B_1^+ correction is shown in Figure 24D.

After applying B_1^+ radio-frequency field inhomogeneity correction, the *mean* \pm *SD* T1 relaxation times obtained for the different fat fraction are shown in the second column in Table 17.

To verify the T1 values obtained after B_1^+ radio-frequency field inhomogeneity correction, two IR RARE sequences were employed to measure the signal cancellation in the main vials consisting of 100% FF and a FF value between 10% and 25%, and acquired at inversion recovery times 500 *ms* (see Figure 24F) and 1500 *ms* (see Figure 24E), respectively.

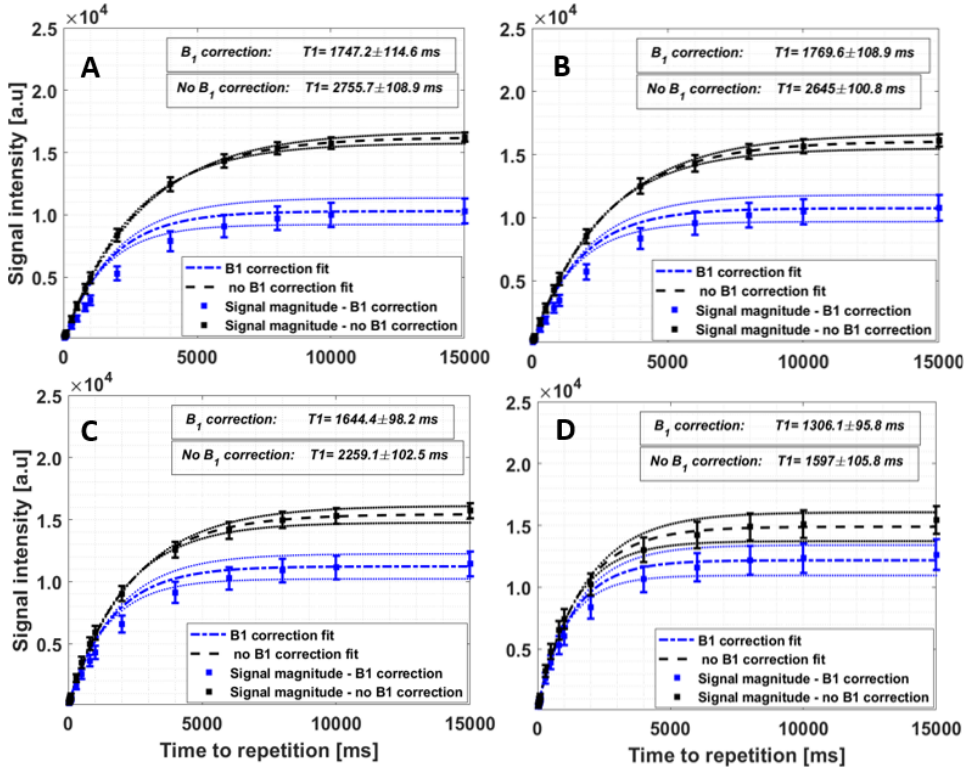


Figure 25: B_1^+ and no B_1^+ corrected T1 fittings of aggregated voxels intensity distribution within each vial. Fittings include, fitting curve (eq. 26) with mean M_0 , T1 and additive error of aggregated voxels intensity distribution and its 95% CI. Errorbars with the mean and *1SD* of aggregated voxels intensity distribution are also represented for both B_1^+ and no B_1^+ corrected values. A: 0% fat content (vial 6 in Figure 24); B: 2% fat content (vial 5 in Figure 24); C: 10% fat content (vial 4 in Figure 24); D: 25% fat content (vial 3 in Figure 24).

The T1 fittings of aggregated voxel intensity distribution within each vial in the Dixon phantom without gadolinium before and after applying B_1^+ cor-

rection are shown in the Figures 25 and 26. The T1 fittings include, fitting curve (equation 22) with mean M_0 , T_1 and additive error of aggregated voxel intensity distribution and its 95% CI. Errorbars with the $mean \pm 1 \cdot SD$ signal intensity of aggregated voxel intensity distribution are also represented for both B_1^+ and no B_1^+ corrected values.

Figure 25A shows the fittings for 0% fat content and corresponds to vial 6 in Figure 24). Figure 25B shows the fittings for 2% fat content and corresponds to vial 5 in Figure 24). Figure 25C shows the fittings for 10% fat content and corresponds to vial 4 in Figure 24). Figure 25D shows the fittings for 25% fat content and corresponds to vial 3 in Figure 24).

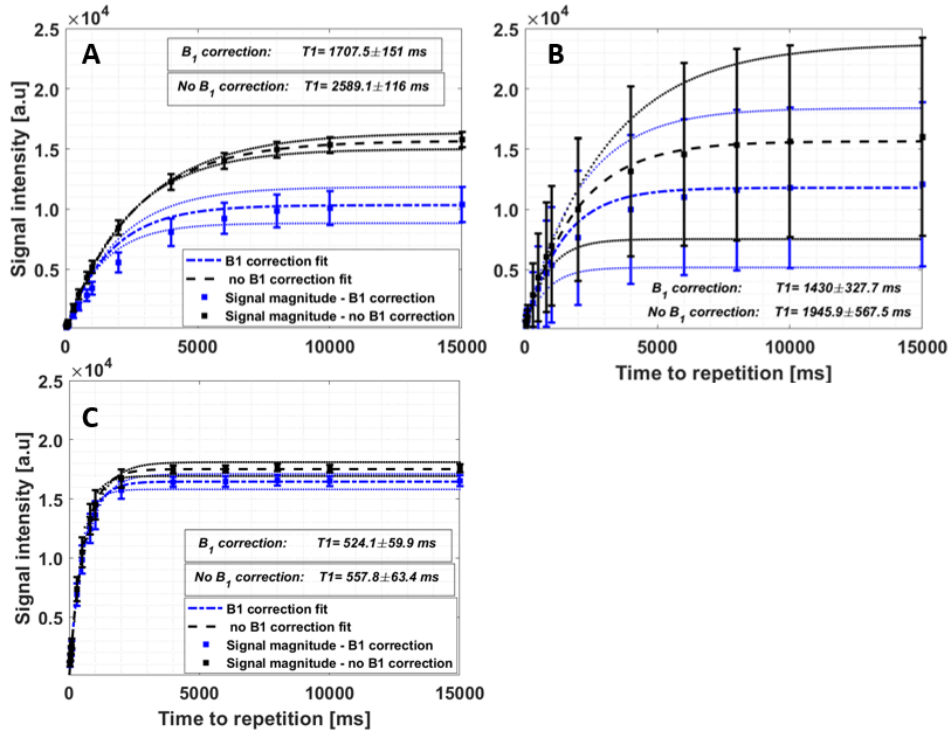


Figure 26: B_1^+ and no B_1^+ corrected T1 fittings of aggregated voxels intensity distribution within each vial. Fittings include, fitting curve (eq. 26) with mean M_0 , T_1 and additive error of aggregated voxels intensity distribution and its 95% CI. Errorbars with the mean and $1SD$ of aggregated voxels intensity distribution are also represented for both B_1^+ and no B_1^+ corrected values. A: 50% fat content (vial 1 in Figure 24); B: 50% fat content (vial 2 in Figure 24); C: 100% fat content (vial 7 in Figure 24).

Figure 26A shows the fittings for 50% fat content and corresponds to vial 1 in Figure 24). Figure 26B shows the fittings for 50% fat content and corresponds to vial 2 in Figure 24). Figure 26C shows the fittings for 100% fat content and corresponds to vial 7 in Figure 24).

T2 mapping

The magnitude image of the mean of all echo images in the MSME acquisition for the Dixon phantom without Gd is shown in Figure 27A.

The T2 relaxation times obtained after fitting voxel-wise the signal intensity to equation 26 are shown in Table 18. And the T2 map for the Dixon phantom without gadolinium is shown in Figure 27B.

Table 18: T2 relaxation times of the different solutions in the Dixon phantom without gadolinium.

	T_2 [ms]
0% FF	36.3 ± 1.3
2% FF	34.7 ± 1.8
10% FF	35.9 ± 1.2
25% FF	43.3 ± 8.1
50% FF	46.1 ± 1.7
50% FF	34.0 ± 1.6
100% FF	64.8 ± 0.5

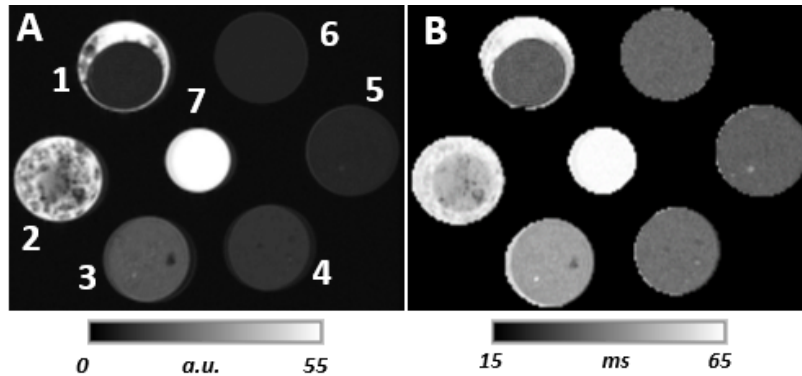


Figure 27: A: Magnitude image of the mean of all echo images in the MSME acquisition; B: T2 map. The different vials are: 1- 50% fat content; 2- 50% fat content; 3- 25% fat content; 4-10% fat content; 5-2% fat content; 6-0% fat content; 7-100% fat content.

From Table 18 and not taking into account the 50% fat content results since as discussed before they have unknown fat content, it can be seen that the T2 relaxation time doesn't decrease with increasing fat content, as it should be expected. This is due to the high agarose content. It has been shown that increasing agarose concentration decreases T2 relaxation times

[88]. Both increasing fat and agarose concentration have the same shortening effect on T2 relaxation time. Therefore the different combination of agarose (in water solution) and fat fractions make difficult to compare the T2 relaxation times shown in 17.

The T2 fittings of aggregated voxels intensity distribution within each vial in the Dixon phantom without gadolinium are shown in Figure 28 and Figure 29. The fittings include, fitting curve (equation 26) with mean M_0 , T_2 and additive error of aggregated voxels intensity distribution and its 95% CI.

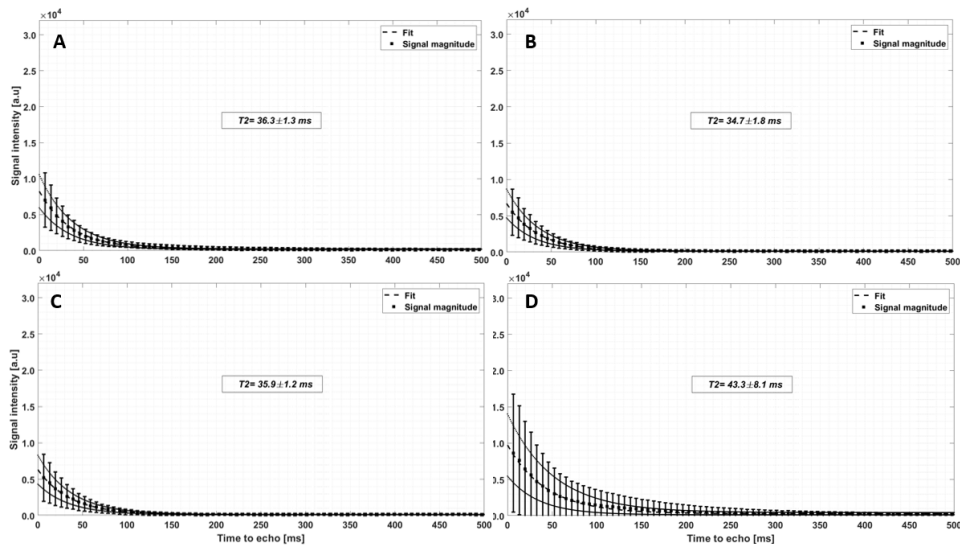


Figure 28: T2 fittings of aggregated voxels intensity distribution within each vial. Fittings include, fitting curve (eq. 26) with mean M_0 , T_2 and additive error of aggregated voxels intensity distribution and its 95% CI. Errorbars with the mean and 1SD of aggregated voxels intensity distribution are also plotted. A: 0% fat content (vial 6 in Figure 24); B: 2% fat content (vial 5 in Figure 24); C: 10% fat content (vial 4 in Figure 24); D: 25% fat content (vial 3 in Figure 24).

Errorbars with the $mean \pm 1 \cdot SD$ signal intensity of aggregated voxels are also plotted.

Figure 28A shows the T2 fittings of aggregated voxels intensity distribution for 0% fat content and corresponds to vial 6 in Figure 27). Figure 28B shows the T2 fittings of aggregated voxels intensity distribution for 2% fat content and corresponds to vial 5 in Figure 27). Figure 28C shows the T2 fittings of aggregated voxels intensity distribution for 10% fat content and corresponds to vial 4 in Figure 27). Figure 28D shows the T2 fittings of aggregated voxels intensity distribution for 25% fat content and corresponds to vial 3 in Figure 27).

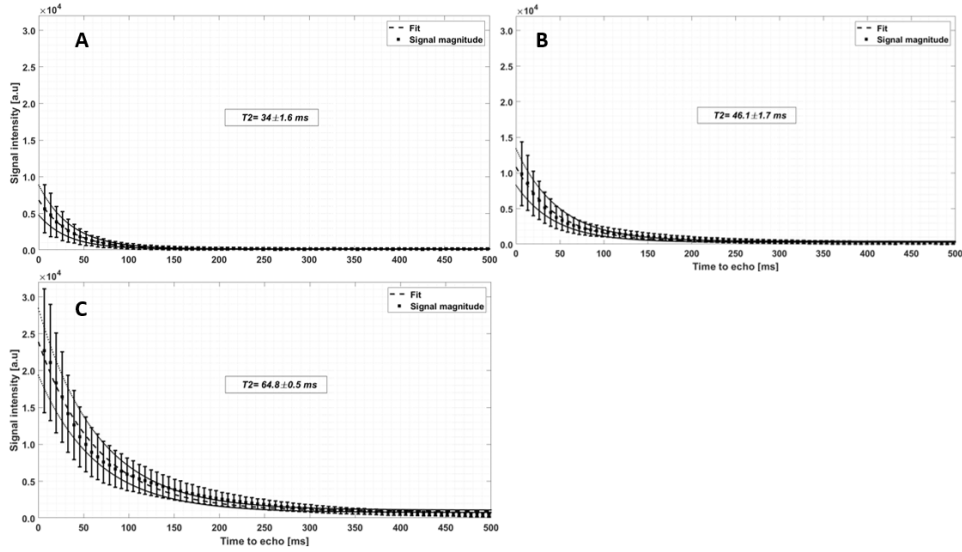


Figure 29: T2 fittings of aggregated voxels intensity distribution within each vial. Fittings include, fitting curve (eq. 26) with mean M_0 , T_2 and additive error of aggregated voxels intensity distribution and its 95% CI. Errorbars with the mean and $1SD$ of aggregated voxels intensity distribution are also plotted. A: 50% fat content (vial 1 in Figure 24); B: 50% fat content (vial 2 in Figure 24); C: 100% fat content (vial 7 in Figure 24).

Figure 29A shows the T2 fittings of aggregated voxels intensity distribution for 50% fat content and corresponds to vial 1 in Figure 27). Figure 29B shows the T2 fittings of aggregated voxels intensity distribution for 50% fat content and corresponds to vial 2 in Figure 27). Figure 29C shows the T2 fittings of aggregated voxels intensity distribution for 100% fat content and corresponds to vial 7 in Figure 27).

Dixon IDEAL algorithm

From the 6–point Dixon sequence, we calculated the water and fat fractions using the complete 6 echoes set of the MGE acquisition; using the first four echoes and using the last for echoes under the assumptions of 0, 1, 2 and 6 fatty acids double bonds. The obtained FF (in %) for the different sequences and under the assumption of 0, 1, 2 and 6 fatty acids double bonds are shown in Table 19.

In general, the sequence including all 6 echoes fails to depict the correct fat content, except for the 25% fat content under the assumption of 0 fatty acids double bonds. The first four echoes and the last four echoes sequences manage to depict the correct fat content under the correct number of fatty

Table 19: Dixon phantom without gadolinium Dixon results. Fat fractions (FF) (in %) estimated under the assumption of 0, 1, 2 and 6 fatty acids double bonds (D.B) for the different echoes combinations.

	D.B	0% FF(%)	2% FF(%)	10% FF(%)	25% FF(%)	50% FF(%)	50% FF(%)	100% FF(%)
1 st -4 th echoes	0	3.12	2.28	5.29	26.72	3.59	1.99	36.79
	1	3.53	2.82	5.58	29.24	3.36	2.39	64.39
	2	4.14	3.61	6.23	29.14	3.76	3.10	78.69
	6	4.92	5.19	7.63	11.57	6.45	5.04	40.25
3 rd -6 th echoes	0	2.47	2.38	3.07	23.35	10.75	2.87	99.95
	1	2.67	2.52	3.59	29.85	13.07	3.19	96.36
	2	2.88	2.66	4.26	29.49	15.46	3.53	70.05
	6	3.48	3.15	5.74	26.98	25.38	4.77	8.55
All 6 echoes	0	1.34	1.23	1.67	17.16	5.12	1.10	0.19
	1	1.44	1.28	0.98	12.79	5.08	1.02	0.17
	2	2.01	2.04	0.79	0.88	6.34	1.52	0.47
	6	2.01	2.04	0.79	0.88	6.34	1.52	0.47

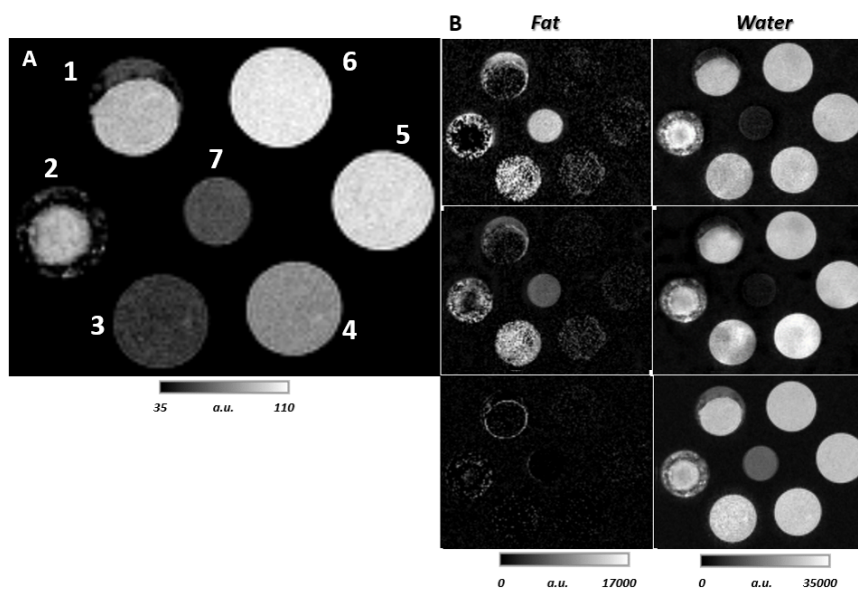


Figure 30: Dixon phantom without gadolinium Dixon results. A: Magnitude image of the sum of all 6 echoes of the MGE acquisition. B: Only-fat (Fat column) and only-water (Water column) images of the Dixon phantom under the assumption of 2 fatty acids double bonds. Top row: first four echoes image; middle row: last four echoes image; bottom row: all 6 echoes image. The different vials are: 1- 50% fat content; 2- 50% fat content; 3- 25% fat content; 4-10% fat content; 5-2% fat content; 6-0% fat content; 7-100% fat content.

acids double bonds assumptions. They especially perform good for fat content above 10%, except for the two 50% fat content cases where the water and fat solutions didn't emulsify correctly. The last four echoes sequence performs better than the first four echoes sequence at depicting the correct fat content for 25% and 100% fat content, whereas the first four echoes sequence performs better than the last four echoes sequence for the 10% fat content. All sequences overestimate the 0% fat content solution obtaining fat fractions quite similar to those obtained for the 2% fat content.

Overall, the best and most stable results are obtained under the assumption of 1 and 2 fatty acids double bonds.

A magnitude image of the sum of all 6 echoes of the MGE acquisition for the Dixon phantom without gadolinium is shown in Figure 30A.

The water-only and fat-only images of the Dixon phantom without Gd under the assumption of 2 fatty acids double bonds are shown in Figure 30B, in Fat and Water columns, respectively. The top row corresponds to the first four echoes images, the middle row corresponds to the last four echoes images and the bottom row corresponds to all 6 echoes images.

5 Discussion

In the current project, an analysis and validation of a proposed non-invasive glymphatic MR protocol at 9.4 T was performed. The protocol consisted of diffusion-weighted imaging (DWI) based on echo-planar imaging (EPI) approach for assessment of free water molecules mobility, along with Dixon imaging based on fast multiple gradient-echo (MGE) sequence for non-invasive assessment of water content within the brain parenchyma of AQP4 KO and WT littermate animals.

Performed analysis revealed usefulness of proposed non-invasive approach in assessment of microscopic differences in the brain morphology between animals devoid of main water transport channel AQP4 compared to normal conditions. First, capability of proposed DWI approach, using measured 17 b-values in range from 0–2000 s/mm^2 , in revealing subtle differences in slow diffusion markers, as apparent-diffusion coefficient (ADC, see section 4.1.1) using monoexponential and intravoxel incoherent motion diffusion (D) using biexponential approaches (see section 4.1.1). These differences reflected both higher ADC and D in KO mice, by means of both acquisition with 22 ms and 30 ms echo times (TE). Although MR images acquired with longer TE were affected by lower signal-to-noise ratio (not assessed here), such approach provided more consistent findings between ADC and D and revealed KO vs. WT differences among around two times more (significant difference was depicted in 5 ROIs in DWI at 22 ms vs. 8 ROIs in DWI at 30 ms) parenchymal regions (see Tables 9 and 10). This might likely be caused by DWI images acquired with 30 ms TE having decreased influence of ghosting artifact compared to those in 22 ms TE images. On the other hand, it may also suggest existence of slightly higher influence of proton density signal in lower vs. higher echo images. Higher contribution from not fully saturated vascular signal may also be considered in the lower TE images, although saturation bands were applied to cancel the arterial input as well as possible motion artifacts from underside of the animal’s head. Therefore, applicability of higher TE DWI over the state-of-the-art approach was confirmed specifically for the glymphatic imaging (see section 4.1).

To further bring closer an idea of fully non-invasive glymphatic protocol, an analysis and validation of Dixon fat and water imaging was performed based on provided images. The images consisted of 6-echoes MGE acquisitions, and calculation was performed using 4 different assumption of fat/water brain compositions (see section 3.2.2). In the original hypothesis, Dixon was supposed to provide information on 1) rather static components of the brain fat/water content, and 2) using fully non-invasive approach without a need in applying invasive procedures. To validate our hypothesis, Dixon parameter optimization was performed both in live animals and phan-

toms. The results obtained using a dedicated IDEAL algorithm [47, 48] were further validated in the phantoms of different fat/water compositions. As AQP4 channels are heterogeneously expressed in the mouse brain [23], therefore a local difference in water content between KO and WT animals was foreseen in different brain regions. The largest difference was found in the periaqueductal gray ($mean\ KO - mean\ WT \pm standard\ error\ of\ the\ mean = 1.69\% \pm 0.70\%$) using the 6-echoes MGE acquisition under 2 fatty acids double bonds. Existence of region-wise correlation between mean water fraction (WF) and mean D in WT but not KO suggests lack of AQP4 reducing brain water heterogeneity in KO mice compared to that in WT. Still, correlation in WT could be due to the small size group (only 4 WTs) compared to a larger size in KO (6 KOs) so this topic requires further analysis in a larger cohort of animals.

Above findings provide novel information for the glymphatics research, on intrinsic fluid behaviour. Still, any biomedical analysis method is a superposition of the biological phenomena and the measurements method so to provide validation for the above Dixon results, an additional validation was performed in the phantoms. The phantoms, of own author's design, were of 3 groups: 1) 'water' phantom with gadobutrol (section 4.3.1); 2) 'fat/water' Dixon phantom including gadobutrol (section 4.3.2); 3) 'fat/water' Dixon phantom without gadobutrol (section 4.3.3). MGE images acquired for each were analyzed using all Dixon computational approaches applied in *in-vivo* scans (see section 3.2.2). For the first 'water' phantom, addition of gadolinium into the aCSF showed that the acquired MR signals can provide bias resulting in IDEAL algorithm depicting fat signal in their absence (see Table 13). Although negligible bias, estimating the fat fraction $< 1\%$, existed for sole aCSF solution, it may be attributed to the principle of Dixon method assuming fat and water signals summing up to 100%. The results closest to aCSF conditions were observed for the aCSF $+0.001\ mM/mL$ solution. This solution is not only close to that predominantly used for glymphatics using DCE approach [26, 89], but also provided optimal T1 and T2 signal shortening for the proposed MR protocol (see section 3.3.1, and Figures 12 and 14). Both higher and lower gadobutrol concentrations increased estimation of fat content within the solution of up to 3%. Therefore, a question appeared on how accurate the estimation of low FF would be in presence gadolinium contamination.

The results obtained with the second phantom – Dixon phantom with gadolinium – and third phantom – Dixon without gadolinium – confirmed that the bias from the tracer can misestimate the fat content. This misestimation was even larger in the 3% agarose than sole aCSF solution (Table 16 aCSF $+0.001\ mM/mL$ vs. 0% FF). Moreover, separation of the original 6-echoes MGE into two 4-echoes image sequences provides better result for

estimation of low and high fat content (see Table 16). The best estimates were obtained for the pure oil solution (100% FF, which doesn't include gadobutrol) using 3rd – 6th echo train (see Table 16), while total fat-water swap was observed using 6–echoes (both assuming presence of 0 and 1 fatty acids double bonds). Slightly worse estimates were obtained using 1st – 4th echo train (see Table 16) for the 25% FF solutions assuming the same number of double bonds. 2% FF was the best estimated using the same echo train, but assuming 6 double bonds, while 0% FF had constant bias < 3% which, on the other hand is typical for a Dixon method [48]. On the other hand, lack of gadolinium in the phantom of the same way prepared fat and agarose solutions provided much better estimates of all FF (except 50%, which was not homogeneous; see section 3.3.3). Acceptable estimates of fat content < 25% were obtained again using 1st – 4th echo train approach, while the high fat content (100%, pure oil) using 3rd – 6th echo train. Still, a global fat-water swap was still visible for 100% fat content vial, using a 6–echoes approach. 2% FF was overall estimated similarly using all approaches. Summarizing, addition of gadolinium results in slight increase of the estimated FF. This suggest that MR signal shortening due to gadolinium may destroy signal from larger number of fatty acids double bonds (see Table 16 vs. 19) or mimic the fat signal, unsuitably for the Dixon. This bias is expected to be higher in case of sub-optimal signal shortening for current TE and TR Dixon setup (see Tables 2, 4, 6 and 8), i.e. higher and lower than 0.001 mM/mL gadobutrol concentrations (see Table 13). However, the best verification would be empirical and possibly performed in the future.

Current work has also limitations. First, an EPI approach was applied for DWI *in-vivo*. However using pulse gradient SE [90] approach would provide better signal-to-noise ratio (SNR), lack of ghosting artifacts and results in better ROI segmentation. Still, it would also have much longer acquisition time (> 2 hours) not reasonable for live animal imaging. In case of breath-controlled acquisition applied for the original data, it would weaken the physiological stability of the recordings due to need in long anesthesia. Second, *in-vivo* Dixon images used in this work were of relatively low resolution (see Table 2), which made additionally the manually performed segmentation less precise. Third, small group size, especially from the complete DWI + Dixon protocol (6 KOs and 4 WTs) provided made both statistical and correlational analyses quite susceptible to randomness. To overcome these limitations, acquisition of additional DWI and Dixon *in-vivo* images would be desired. Furthermore, it would be preferred to acquire Dixon images with both higher resolution and SNR, which in turn will increase the scan time. Still assessment of both *in-vivo* and *ex-vivo* images SNR was not included into the current work, as its main aim was to analyse and confirm the usability of proposed idea for non-invasive glymphatic MR approach. Also, lack of larger animal cohort was overcome with application of non-parametric sta-

tistical approach.

Nevertheless, presented non-invasive approach to glymphatic MRI rather overcomes the above limitations as shows application of powerful tools, especially for future translational glymphatic research. Glymphatic function is physiologically regulated, however it is currently understood only through the lens of solute exchange using predominantly invasive methods, i.e., DCE-MRI. There is a strong need in this gold-standard tracer-based measurements both in rodents and in humans, to validate our non-invasive approach. Hence, once feasibility of non-invasive approach would be validated, such protocol can be implemented into the clinical research and further clinical diagnostics to identify the brain condition in patients.

In this project we used AQP4 KO transgenic mice, but future research should also encompass animal disease models already known as showing glymphatic impairment, e.g. Alzheimer's disease [91] or hydrocephalus [92]. Presented here protocol was also designed based on widely available sequence among all clinical MR scanners. Both DWI and Dixon have already its place established in neurological, oncological and neuromuskular assessment. Therefore, a high usability of current protocol might be foreseen in clinical diagnostics of stroke, is also necessary to validate our clinical potential for non-invasive glymphatic assessment [93].

Future perspectives

Based on the phantoms imaging results, the nearest future works on non-invasive glymphatic MRI should investigate the results obtained by using the first four echoes and last four echoes sequences for the analyzed here Dixon *in-vivo* imaging. This way, a new modifications providing faster and higher resolution imaging might be designed, and bringing even closer applicability of the protocol in clinical setups.

Increase in resolution should be simultaneously addressed with increase in SNR - especially important for the *in-vivo* imaging. Furthermore, both DWI and Dixon acquisition should be verified in electrocardiogram-mode apart from the respiratory-gated mode. This way, the presented validation might be concluded for future translational steps.

6 Conclusions

Concluding, current work confirmed applicability of the proposed fully non-invasive glymphatic protocol in revealing subtle changes in the brain water mobility and content using DWI and Dixon imaging. It was shown that application of longer echo time of 30 *ms* for DWI provides more stable and consistent results. This refers to both ADC and IVIM models applied. Furthermore, applied Dixon imaging along with processing pipeline allowed to distinguish subtle differences in the brain water content in KO vs. WT animals. Although these results might be of dispute and require additional validation, our results in *ex-vivo* Dixon phantoms (with and without gadolinium) suggests that increasing number of echo images does not necessarily improve the Dixon technique performance. Therefore, it is foreseen that findings in mice shall be confirmed by recalculating all *in-vivo* images based on the phantoms imaging results. Therefore, the nearest future work should consider investigating the results obtained in *in-vivo* by using separately only the first four echoes and last four echoes sequences for Dixon imaging.

References

- [1] L M Oliveira, E G Figueiredo, and C M Albuquerque Peres. The Glymphatic System: A Review. *Arquivos Brasileiros de Neurocirurgia: Brazilian Neurosurgery*, 37(03):190–195, 2018.
- [2] Z Wang, Z Ying, A Bosy-Westphal, J Zhang, M Heller, W Later, S B Heymsfield, and M J Müller. Evaluation of Specific Metabolic Rates of Major Organs and Tissues: Comparison Between Nonobese and Obese Women. *Obesity*, 20(1):95–100, 2012.
- [3] M Nedergaard. Garbage truck of the brain. *Science*, 340(6140):1529–1530, 2013.
- [4] WH Oldendorf and H Davson. Brain extracellular space and the sink action of cerebrospinal fluid. *Transactions of the American Neurological Association*, 92:123–127, 1967.
- [5] L Sakka, G Coll, and J Chazal. Anatomy and physiology of cerebrospinal fluid. *European annals of otorhinolaryngology, head and neck diseases*, 128(6):309–316, 2011.
- [6] T Brinker, E Stopa, J Morrison, and P Klinge. A new look at cerebrospinal fluid circulation. *Fluids and Barriers of the CNS*, 11(1):1–16, 2014.
- [7] L Xie, H Kang, Q Xu, M J Chen, Y Liao, M Thiyagarajan, J O’Donnell, D J Christensen, C Nicholson, J J Iliff, et al. Sleep drives metabolite clearance from the adult brain. *science*, 342(6156):373–377, 2013.
- [8] J J Iliff, M Wang, Y Liao, B A Plogg, W Peng, G A Gundersen, H Benveniste, G E Vates, R Deane, S A Goldman, E A Nagelhus, and M Nedergaard. A Paravascular Pathway Facilitates CSF Flow through the Brain Parenchyma and the Clearance of Interstitial Solutes, Including Amyloid β . *Science Translational Medicine*, 4(147), 2012.
- [9] N A Jessen, A S F Munk, I Lundgaard, and M Nedergaard. The glymphatic system: a beginner’s guide. *Neurochemical research*, 40(12):2583–2599, 2015.
- [10] A S Thrane, V R Thrane, and M Nedergaard. Drowning stars: reassessing the role of astrocytes in brain edema. *Trends in Neurosciences*, 37(11):620–628, 2014.
- [11] C E Johanson. Choroid plexus–cerebrospinal fluid circulatory dynamics: impact on brain growth, metabolism, and repair. In *Neuroscience in medicine*, pages 173–200. Springer, 2008.

- [12] R C Besing, J R Paul, L M Hablitz, C O Rogers, R L Johnson, M E Young, and K L Gamble. Circadian rhythmicity of active GSK3 isoforms modulates molecular clock gene rhythms in the suprachiasmatic nucleus. *Journal of biological rhythms*, 30(2):155–160, 2015.
- [13] H Lee, L Xie, M Yu, H Kang, T Feng, R Deane, J Logan, M Nedergaard, and H Benveniste. The effect of body posture on brain glymphatic transport. *Journal of Neuroscience*, 35(31):11034–11044, 2015.
- [14] I Lundgaard, W Wang, A Eberhardt, H S Vinitzky, B C Reeves, S Peng, N Lou, R Hussain, and M Nedergaard. Beneficial effects of low alcohol exposure, but adverse effects of high alcohol intake on glymphatic function. *Scientific reports*, 8(1):1–16, 2018.
- [15] S von Holstein-Rathlou, N C Petersen, and M Nedergaard. Voluntary running enhances glymphatic influx in awake behaving, young mice. *Neuroscience letters*, 662:253–258, 2018.
- [16] J H Ahn, H Cho, J Kim, S H Kim, J Ham, I Park, S H Suh, S P Hong, J Song, Y Hong, et al. Meningeal lymphatic vessels at the skull base drain cerebrospinal fluid. *Nature*, 572(7767):62–66, 2019.
- [17] X Cai, J Qiao, P Kulkarni, I C Harding, E Ebong, and C F Ferris. Imaging the effect of the circadian light–dark cycle on the glymphatic system in awake rats. *Proceedings of the National Academy of Sciences*, 117(1):668–676, 2020.
- [18] J J Iliff, H Lee, M Yu, T Feng, J Logan, M Nedergaard, H Benveniste, et al. Brain-wide pathway for waste clearance captured by contrast-enhanced MRI. *The Journal of clinical investigation*, 123(3):1299–1309, 2013.
- [19] H Lee, K Mortensen, S Sanggaard, P Koch, H Brunner, B Quistorff, M Nedergaard, and H Benveniste. Quantitative Gd-DOTA uptake from cerebrospinal fluid into rat brain using 3D VFA–SPGR at 9.4 T. *Magnetic resonance in medicine*, 79(3):1568–1578, 2018.
- [20] P Agre. The Aquaporin Water Channels. *Proceedings of the American Thoracic Society*, 3(1):5–13, 2006.
- [21] H Mestre, L M Hablitz, A L R Xavier, W Feng, W Zou, T Pu, H Monai, G Murlidharan, R M C Rivera, M J Simon, et al. Aquaporin-4-dependent glymphatic solute transport in the rodent brain. *Elife*, 7:e40070, 2018.
- [22] C Iacovetta, E Rudloff, and R Kirby. The role of aquaporin 4 in the brain. *Veterinary Clinical Pathology*, 41(1):32–44, 2012.

- [23] J A Hubbard, M S Hsu, M M Seldin, and D K Binder. Expression of the astrocyte water channel aquaporin-4 in the mouse brain. *ASN neuro*, 7(5):1759091415605486, 2015.
- [24] L Xie, H Kang, Q Xu, M J Chen, Y Liao, M Thiyagarajan, J O'Donnell, D J Christensen, C Nicholson, J J Iliff, T Takano, R Deane, and M Nedergaard. Sleep Drives Metabolite Clearance from the Adult Brain. *Science*, 342(6156):373–377, 2013.
- [25] W J Strittmatter. Bathing the brain. *Journal of Clinical Investigation*, 123(3):1013–1015, 2013.
- [26] E H Stanton, N D Å Persson, R S Gomolka, T Lilius, B Sigurdsson, H Lee, A L R Xavier, H Benveniste, M Nedergaard, and Y Mori. Mapping of CSF transport using high spatiotemporal resolution dynamic contrast-enhanced MRI in mice: effect of anesthesia. *Magnetic Resonance in Medicine*, 85(6):3326–3342, 2021.
- [27] J J Iliff, M Wang, D M Zeppenfeld, A Venkataraman, B A Plog, Y Liao, R Deane, and M Nedergaard. Cerebral arterial pulsation drives paravascular CSF–interstitial fluid exchange in the murine brain. *Journal of Neuroscience*, 33(46):18190–18199, 2013.
- [28] L Yang, B T Kress, H J Weber, M Thiyagarajan, B Wang, R Deane, H Benveniste, J J Iliff, and M Nedergaard. Evaluating glymphatic pathway function utilizing clinically relevant intrathecal infusion of CSF tracer. *Journal of Translational Medicine*, 11(1), 2013.
- [29] J J Iliff, M J Chen, B A Plog, D M Zeppenfeld, M Soltero, L Yang, I Singh, R Deane, and M Nedergaard. Impairment of Glymphatic Pathway Function Promotes Tau Pathology after Traumatic Brain Injury. *The Journal of Neuroscience*, 34(49):16180–16193, 2014.
- [30] W Peng, T M Achariyar, B Li, Y Liao, H Mestre, E Hitomi, S Regan, T Kasper, S Peng, F Ding, H Benveniste, M Nedergaard, and R Deane. Suppression of glymphatic fluid transport in a mouse model of Alzheimer's disease. *Neurobiology of Disease*, 93:215–225, 2016.
- [31] B T Kress, J J Iliff, M Xia, M Wang, H S Wei, D Zeppenfeld, L Xie, H K, Q Xu, J A Liew, B A Plog, F Ding, R Deane, and M Nedergaard. Impairment of paravascular clearance pathways in the aging brain. *Annals of Neurology*, 76(6):845–861, 2014.
- [32] A M Sweeney, Plá, T Du, G Liu, Q Sun, S Peng, B A Plog, B T Kress, X Wang, H Mestre, et al. In vivo imaging of cerebrospinal fluid transport through the intact mouse skull using fluorescence macroscopy. *JoVE (Journal of Visualized Experiments)*, (149):e59774, 2019.

- [33] V Gulani, F Calamante, F G Shellock, E Kanal, and S B Reeder. Gadolinium deposition in the brain: summary of evidence and recommendations. *The Lancet Neurology*, 16(7):564–570, 2017.
- [34] ME Moseley, C Liu, S Rodriguez, and T Brosnan. Advances in magnetic resonance neuroimaging. *Neurologic Clinics*, 27(1):1–24, 2009.
- [35] G S Chilla, C H Tan, C Xu, and C L Poh. Diffusion weighted magnetic resonance imaging and its recent trend—a survey. *Quantitative imaging in medicine and surgery*, 5(3):407, 2015.
- [36] J E Tanner and E O Stejskal. Restricted self-diffusion of protons in colloidal systems by the pulsed-gradient, spin-echo method. *The Journal of Chemical Physics*, 49(4):1768–1777, 1968.
- [37] T Tsurugizawa, L Ciobanu, and D Le Bihan. Water diffusion in brain cortex closely tracks underlying neuronal activity. *Proceedings of the National Academy of Sciences*, 110(28):11636–11641, 2013.
- [38] Y Assaf, H Johansen-Berg, and M Thiebaut de Schotten. The role of diffusion MRI in neuroscience. *NMR in Biomedicine*, 32(4):e3762, 2019.
- [39] H Mestre, T Du, A M Sweeney, G Liu, A J Samson, W Peng, K N Mortensen, F F Stæger, P AR Bork, L Bashford, et al. Cerebrospinal fluid influx drives acute ischemic tissue swelling. *Science*, 367(6483):eaax7171, 2020.
- [40] V Baliyan, C J Das, R Sharma, and A K Gupta. Diffusion weighted imaging: technique and applications. *World journal of radiology*, 8(9):785, 2016.
- [41] T Taoka and S Naganawa. Glymphatic imaging using MRI. *Journal of Magnetic Resonance Imaging*, 51(1):11–24, 2020.
- [42] Ş B Demiral, D Tomasi, J Sarlls, H Lee, C E Wiers, A Zehra, T Srivastava, K Ke, E Shokri-Kojori, C R Freeman, et al. Apparent diffusion coefficient changes in human brain during sleep—Does it inform on the existence of a glymphatic system? *NeuroImage*, 185:263–273, 2019.
- [43] I F Harrison, B Siow, A B Akilo, P G Evans, O Ismail, Y Ohene, P Nahavandi, D L Thomas, M F Lythgoe, and J A Wells. Non-invasive imaging of CSF-mediated brain clearance pathways via assessment of perivascular fluid movement with diffusion tensor MRI. *Elife*, 7:e34028, 2018.
- [44] G B Chavhan, P S Babyn, B G Jankharia, H M Cheng, and M M Shroff. Steady-state MR imaging sequences: physics, classification, and clinical applications. *Radiographics*, 28(4):1147–1160, 2008.

- [45] W T Dixon. Simple proton spectroscopic imaging. *Radiology*, 153(1):189–194, 1984.
- [46] A Haase, J Frahm, D Matthaei, W Hanicke, and K-D Merboldt. FLASH imaging. Rapid NMR imaging using low flip-angle pulses. *Journal of Magnetic Resonance (1969)*, 67(2):258–266, 1986.
- [47] J Tsao and Y Jiang. Hierarchical IDEAL: robust water-fat separation at high field by multiresolution field map estimation. In *Proceedings of the International Society for Magnetic Resonance in Medicine*, volume 16, page 653, 2008.
- [48] Y Jiang and J Tsao. Fast and robust separation of multiple chemical species from arbitrary echo times with complete immunity to phase wrapping. In *Proceedings of the 20th Annual Meeting of ISMRM*, volume 388, 2012.
- [49] R H Hashemi, W G Bradley, and C J Lisanti. *MRI: the basics: The Basics*. Lippincott Williams & Wilkins, 2012.
- [50] D Le Bihan, E Breton, D Lallemand, P Grenier, E Cabanis, and M Laval-Jeantet. MR imaging of intravoxel incoherent motions: application to diffusion and perfusion in neurologic disorders. *Radiology*, 161(2):401–407, 1986.
- [51] D Le Bihan, E Breton, D Lallemand, M L Aubin, J Vignaud, and M Laval-Jeantet. Separation of diffusion and perfusion in intravoxel incoherent motion MR imaging. *Radiology*, 168(2):497–505, 1988.
- [52] J Ma. Dixon techniques for water and fat imaging. *Journal of Magnetic Resonance Imaging: An Official Journal of the International Society for Magnetic Resonance in Medicine*, 28(3):543–558, 2008.
- [53] Y Xiao, R Paudel, J Liu, C Ma, Z Zhang, and S Zhou. Mri contrast agents: Classification and application. *International journal of molecular medicine*, 38(5):1319–1326, 2016.
- [54] J Hennig, A Nauerth, and H Friedburg. RARE imaging: a fast imaging method for clinical MR. *Magnetic resonance in medicine*, 3(6):823–833, 1986.
- [55] M Poustchi-Amin, S A Mirowitz, J J Brown, R C McKinstry, and T Li. Principles and applications of echo-planar imaging: a review for the general radiologist. *Radiographics*, 21(3):767–779, 2001.
- [56] D Le Bihan, E Breton, D Lallemand, P Grenier, E Cabanis, and M Laval-Jeantet. MR imaging of intravoxel incoherent motions: application to diffusion and perfusion in neurologic disorders. *Radiology*, 161(2):401–407, 1986.

- [57] G Fournet, J Li, A M Cerjanic, B P Sutton, L Ciobanu, and D Le Bihan. A two-pool model to describe the IVIM cerebral perfusion. *Journal of Cerebral Blood Flow & Metabolism*, 37(8):2987–3000, 2016.
- [58] C Federau. Intravoxel incoherent motion MRI as a means to measure *in vivo* perfusion: A review of the evidence. *NMR in Biomedicine*, 30(11):e3780, 2017.
- [59] C Vieni, B Ades-Aron, B Conti, E E Sigmund, P Riviello, T M Shepherd, Y W Lui, D S Novikov, and E Fieremans. Effect of intravoxel incoherent motion on diffusion parameters in normal brain. *NeuroImage*, 204:116228, 2020.
- [60] Wikipedia contributors. Chemical shift — Wikipedia, the free encyclopedia. https://en.wikipedia.org/wiki/Chemical_shift, 2022. [Online; accessed 9-May-2022].
- [61] J Frahm, A Haase, W Hänicke, D Matthaei, H Bomsdorf, and T Helzel. Chemical shift selective MR imaging using a whole-body magnet. *Radiology*, 156(2):441–444, 1985.
- [62] H H Hu, P Börnert, D Hernando, P Kellman, J Ma, S Reeder, and C Sirlin. ISMRM workshop on fat–water separation: insights, applications and progress in MRI. *Magnetic resonance in medicine*, 68(2):378–388, 2012.
- [63] K Kuroda, K Oshio, R V Mulkern, and F A Jolesz. Optimization of chemical shift selective suppression of fat. *Magnetic resonance in medicine*, 40(4):505–510, 1998.
- [64] H Mestre, J Tithof, T Du, W Song, W Peng, A M Sweeney, G Olveda, J H Thomas, M Nedergaard, and D H Kelley. Flow of cerebrospinal fluid is driven by arterial pulsations and is reduced in hypertension. *Nature communications*, 9(1):1–9, 2018.
- [65] J H Lee, H Cheong, S S Lee, C K Lee, Y S Sung, J Huh, J Song, and H Choe. Perfusion Assessment Using Intravoxel Incoherent Motion-Based Analysis of Diffusion-Weighted Magnetic Resonance Imaging. *Investigative Radiology*, 51(8):520–528, 2016.
- [66] S B Reeder, A R Pineda, Z Wen, A Shimakawa, H Yu, J H Brittain, G E Gold, C H Beaulieu, and N J Pelc. Iterative decomposition of water and fat with echo asymmetry and least-squares estimation (IDEAL): application with fast spin-echo imaging. *Magnetic Resonance in Medicine: An Official Journal of the International Society for Magnetic Resonance in Medicine*, 54(3):636–644, 2005.

- [67] H H Hu, P Börnert, D Hernando, P Kellman, J Ma, S Reeder, and C Sirin. ISMRM workshop on fat–water separation: insights, applications and progress in MRI. *Magnetic resonance in medicine*, 68(2):378–388, 2012.
- [68] J Ren, I Dimitrov, A D Sherry, and C R Malloy. Composition of adipose tissue and marrow fat in humans by ^1H NMR at 7 Tesla. *Journal of lipid research*, 49(9):2055–2062, 2008.
- [69] R P Bazinet and S Layé. Polyunsaturated fatty acids and their metabolites in brain function and disease. *Nature Reviews Neuroscience*, 15(12):771–785, 2014.
- [70] T Kirchgesner, S Acid, V Perlepe, F Lecouvet, and B Vande Berg. Two-point Dixon fat-water swapping artifact: lesion mimicker at musculoskeletal T2-weighted MRI. *Skeletal radiology*, 49(12):2081–2086, 2020.
- [71] P A Yushkevich, J Piven, H Cody Hazlett, R Gimpel Smith, S Ho, J C Gee, and G Gerig. User-Guided 3D Active Contour Segmentation of Anatomical Structures: Significantly Improved Efficiency and Reliability. *NeuroImage*, 31(3):1116–1128, 2006.
- [72] S M Sunkin, L Ng, C Lau, T Dolbeare, T L Gilbert, C L Thompson, M Hawrylycz, and C Dang. Allen Brain Atlas: an integrated spatio-temporal portal for exploring the central nervous system. *Nucleic Acids Research*, 41(D1):D996–D1008, 2012.
- [73] M Boudreau, C L Tardif, N Stikov, J G Sled, W Lee, and G B Pike. B_1 mapping for bias–correction in quantitative T1 imaging of the brain at 3T using standard pulse sequences. *Journal of magnetic resonance imaging*, 46(6):1673–1682, 2017.
- [74] C H Cunningham, J M Pauly, and K S Nayak. Saturated double–angle method for rapid B_1+ mapping. *Magnetic Resonance in Medicine: An Official Journal of the International Society for Magnetic Resonance in Medicine*, 55(6):1326–1333, 2006.
- [75] E C Bush, A Gifford, C L Coolbaugh, T F Towse, B M Damon, and E B Welch. Fat–water phantoms for magnetic resonance imaging validation: a flexible and scalable protocol. *JoVE (Journal of Visualized Experiments)*, (139):e57704, 2018.
- [76] H Yu, A Shimakawa, C A McKenzie, J H Brittain, and S B Reeder. IDEAL water–fat decomposition with multipeak fat spectrum modeling. In *16th meeting of the International Society for Magnetic Resonance in Medicine, Toronto, Ontario, Canada*, 2008.

- [77] M Özcan and S Seven. Physical and chemical analysis and fatty acid composition of peanut, peanut oil and peanut butter from ÇOM and NC-7 cultivars. *Grasas y aceites*, 54(1):12–18, 2003.
- [78] E R Kandel, J H Schwartz, T M Jessell, S A Siegelbaum, and AJ Hudspeth. Principles of Neural Science, fifth editon. In *Principles of Neural Science*. McGraw-Hill Education, 2013.
- [79] I Vernikouskaya, A Pochert, M Lindén, and V Rasche. Quantitative ^{19}F MRI of perfluoro-15-crown-5-ether using uniformity correction of the spin excitation and signal reception. *Magnetic Resonance Materials in Physics, Biology and Medicine*, 32(1):25–36, 2019.
- [80] P R Delgado, A Kuehne, J S Periquito, J M Millward, A Pohlmann, S Waiczies, and T Niendorf. B_1 inhomogeneity correction of rare mri with transeive surface radiofrequency probes. *Magnetic Resonance in Medicine*, 84(5):2684–2701, 2020.
- [81] S B Reeder, C A McKenzie, A R Pineda, H Yu, A Shimakawa, A C Brau, B A Hargreaves, G E Gold, and J H Brittain. Water–fat separation with IDEAL gradient-echo imaging. *Journal of Magnetic Resonance Imaging: An Official Journal of the International Society for Magnetic Resonance in Medicine*, 25(3):644–652, 2007.
- [82] D D Stark and W G Bradley. *Magnetic Resonance Imaging*. Mosby, 1999.
- [83] H Lu, L M Nagae-Poetscher, X Golay, D Lin, M Pomper, and P CM Van Zijl. Routine clinical brain MRI sequences for use at 3.0 Tesla. *Journal of Magnetic Resonance Imaging: An Official Journal of the International Society for Magnetic Resonance in Medicine*, 22(1):13–22, 2005.
- [84] T O’Reilly and A G Webb. In vivo T1 and T2 relaxation time maps of brain tissue, skeletal muscle, and lipid measured in healthy volunteers at 50 mT. *Magnetic Resonance in Medicine*, 87(2):884–895, 2022.
- [85] R A de Graaf, P B Brown, S McIntyre, T W Nixon, K L Behar, and D L Rothman. High magnetic field water and metabolite proton T1 and T2 relaxation in rat brain in vivo. *Magnetic resonance in medicine: An official journal of the international society for magnetic resonance in medicine*, 56(2):386–394, 2006.
- [86] R Sindi, Y H Wong, C H Yeong, and Z Sun. Development of patient–specific 3D–printed breast phantom using silicone and peanut oils for magnetic resonance imaging. *Quantitative imaging in medicine and surgery*, 10(6):1237, 2020.

- [87] C D Jordan, M Saranathan, N K Bangerter, B A Hargreaves, and G E Gold. Musculoskeletal MRI at 3.0 T and 7.0 T: a comparison of relaxation times and image contrast. *European journal of radiology*, 82(5):734–739, 2013.
- [88] C Gillmann, N Homolka, W Johnen, A Runz, G Echner, A Pfaffenberger, P Mann, V Schneider, A L Hoffmann, E GC Troost, et al. ADAM PETer—An anthropomorphic, deformable and multimodality pelvis phantom with positron emission tomography extension for radiotherapy. *Medical physics*, 48(4):1624–1632, 2021.
- [89] K N Mortensen, S Sanggaard, H Mestre, H Lee, S Kostrikov, A L R Xavier, A Gjedde, H Benveniste, and M Nedergaard. Impaired glymphatic transport in spontaneously hypertensive rats. *Journal of Neuroscience*, 39(32):6365–6377, 2019.
- [90] E O Stejskal and J E Tanner. Spin diffusion measurements: spin echoes in the presence of a time-dependent field gradient. *The journal of chemical physics*, 42(1):288–292, 1965.
- [91] B C Reeves, J K Karimy, A J Kundishora, H Mestre, H M Cerci, C Matouk, S L Alper, I Lundgaard, M Nedergaard, and K T Kahle. Glymphatic system impairment in Alzheimer’s disease and idiopathic normal pressure hydrocephalus. *Trends in molecular medicine*, 26(3):285–295, 2020.
- [92] C Tan, X Wang, Y Wang, C Wang, Z Tang, Z Zhang, J Liu, and G Xiao. The pathogenesis based on the glymphatic system, diagnosis, and treatment of idiopathic normal pressure hydrocephalus. *Clinical Interventions in Aging*, 16:139, 2021.
- [93] T Gaberel, C Gakuba, R Goulay, S M De Lizarrondo, J Hanouz, E Emery, E Touze, D Vivien, and M Gauberti. Impaired glymphatic perfusion after strokes revealed by contrast-enhanced MRI: a new target for fibrinolysis? *Stroke*, 45(10):3092–3096, 2014.

List of Figures

1	Figure: Glymphatic system	7
2	Figure: Number of published papers	7
3	Figure: Coordinate system	11
4	Figure: GRE diagram	15
5	Figure: Multi-slice acquisition	17
6	Figure: SE and EPI PSD	19
7	Figure: Age and body weight	26

8	Figure: Dixon phantom with gadolinium	33
9	Figure: Dixon phantom without gadolinium	34
10	Figure: Phantom ROIs	41
11	Figure: Dixon WF results	46
12	Figure: Water Phantom T1 results	49
13	Figure: Water Phantom T1 fits	50
14	Figure: Water Phantom T2 images	51
15	Figure: Water Phantom T2 fittings	52
16	Figure: Water Phantom Dixon results	54
17	Figure: Dixon Phantom with gadolinium T1 results	56
18	Figure: Dixon Phantom with gadolinium T1 fittings	57
19	Figure: Dixon Phantom with gadolinium T1 fittings	58
20	Figure: Dixon phantom with gadolinium T2 images	59
21	Figure: Dixon Phantom with gadolinium T2 fittings	59
22	Figure: Dixon Phantom with gadolinium T2 fittings	60
23	Figure: Dixon Phantom with gadolinium Dixon results	62
24	Figure: Dixon Phantom without gadolinium T1 results	64
25	Figure: Dixon Phantom without gadolinium T1 fittings	65
26	Figure: Dixon Phantom without gadolinium T1 fittings	66
27	Figure: Dixon phantom without gadolinium T2 images	67
28	Figure: Dixon Phantom without gadolinium T2 fittings	68
29	Figure: Dixon Phantom without gadolinium T2 fittings	69
30	Figure: Dixon Phantom without gadolinium Dixon results	70